ACSNANO

www.acsnano.org

ARTICLE

Chirality Dependence of Triplet Excitons in (6,5) and (7,5) Single-Wall Carbon Nanotubes Revealed by Optically Detected Magnetic Resonance

Ivan Sudakov, Etienne Goovaerts, Wim Wenseleers, Jeffrey L. Blackburn, Juan G. Duque, and Sofie Cambré*

Cite This: https://doi.org/10.1021/acsnano.2c08392

Read Online

ACCESS | Metrics & More | Article Recommendations | Supporting Information

ABSTRACT: The excitonic structure of single-wall carbon nanotubes (SWCNTs) is chirality dependent and consists of multiple singlet and triplet excitons (TEs) of which only one singlet exciton (SE) is optically bright. In particular, the dark TEs have a large impact on the integration of SWCNTs in optoelectronic devices, where excitons are created electrically, such as in infrared light-emitting diodes, thereby strongly limiting their quantum efficiency. Here, we report the characterization of TEs in chirality-purified samples of (6,5) and (7,5) SWCNTs, either randomly oriented in a frozen solution or with in-plane preferential orientation in a film, by means of optically detected magnetic resonance (ODMR) spectroscopy. In both chiral structures, the nanotubes are shown to sustain three types of TEs. One TE exhibits axial symmetry with zero-field splitting (ZFS) parameters depending on SWCNT diameter, in good agreement with the tighter confinement expected in narrower-diameter nanotubes. The ZFS of this TE also depends on nanotube environment, pointing to slightly weaker confinement for surfactant-coated than for polymer-wrapped SWCNTs. A second TE type, with much smaller ZFS, does not show the same systematic trends with diameter and environment and has a less well-defined axial symmetry. This most likely corresponds to TEs trapped at defect sites at low temperature, as exemplified by comparing SWCNT samples from different origins and after different treatments. A third triplet has unresolved ZFS, implying it originates from weakly interacting spin pairs. Aside from the diameter dependence, ODMR thus provides insights in both the symmetry, confinement, and nature of TEs on semiconducting SWCNTs.

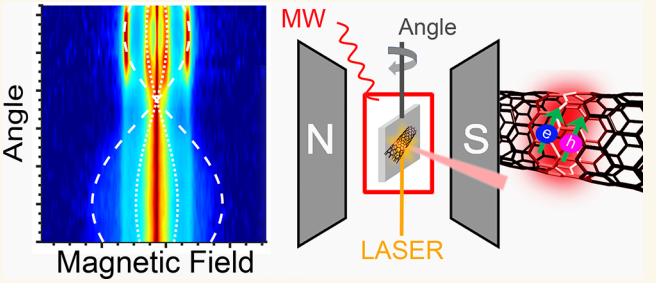

KEYWORDS: *single-wall carbon nanotubes, triplet excitons, optically detected magnetic resonance, chiral structure, zero-field splitting, angular dependence*

The optical and electronic properties of single-wall carbon nanotubes (SWCNTs), which depend critically on their specific chiral structure, have found a large number of promising applications in optoelectronics.[1−3] Due to their quasi-one-dimensional structure, their excited states consist of strongly bound electron−hole pairs (excitons), which can be observed even at room temperature (*i.e.*, binding energies of the order of several hundred meV).[4,5] Since the unit cell of graphene contains two carbon atoms, two equivalent valleys exist in the first Brillouin zone, which result in a complicated exciton fine structure for SWCNTs, with multiple singlet and triplet excitonic states.[6,7] Due to the strong Coulomb coupling, both intravalley and intervalley excitons can be created, where the two intervalley excitons are optically forbidden due to their finite momentum (the so-called K-momentum dark excitons), while intravalley Coulomb interactions give rise to one odd and one even parity singlet exciton (SE), of which only the odd parity exciton is optically allowed (bright exciton). When also spin multiplicity is taken into account, a 16-fold degeneracy is found with 4 SEs and 12 triplet excitons (TEs) of which only the odd parity SE is

Received: August 22, 2022
Accepted: January 11, 2023

optically bright. This imbalance between bright and dark states, combined with efficient exciton transport along the nanotube backbone (*i.e.*, exciton diffusion lengths >100 nm) such that nonradiative recombination can occur at structural defects,[8] results in extremely low fluorescence (PL) quantum efficiencies (typically only a few percent, even in optimized conditions[9−11]). Several strategies have been proposed to enhance this PL quantum yield, *e.g.*, by creating localized potential wells in the nanotube backbone through covalent sp^3-functionalization that trap the otherwise highly mobile excitons,[12−14] thereby preventing nonradiative recombination at quenching defects (even allowing very short SWCNTs to fluoresce brightly[15]), by endohedral functionalization of the SWCNTs with low-dielectric constant solvents,[16,17] by solubilizing long, defect-free and empty SWCNTs without applying any sonication,[9,18] or by breaking the CNT symmetry in a magnetic field and as such brightening the symmetry-forbidden dark excitons.[19]

To stimulate future applications in nanophotonics, a deeper understanding of the role of TEs in the photophysics of SWCNTs is highly needed. In particular for light-emitting devices (LEDs), where excitons are created electrically, dark TEs play a dominant role in limiting the internal quantum efficiency.[14] Without a detailed understanding and control over these TEs, the applicability of SWCNTs in LEDs is strongly hampered, even though their chirality-dependent, narrow-band emission shows great promise for obtaining infrared-emitting LEDs. As shown for other organic LED materials with emission in the infrared,[20] upconversion via triplet−triplet annihilation (TTA) to repopulate excited singlet states or adding spin filters could be employed to harvest the TE emission, which evidences the importance of studying these TEs in SWCNTs. Furthermore, spin-allowed conversion of the dark TEs into bright trions may also serve as a useful radiative pathway.[14] In another promising application, the longer-living triplet states emerge as possible candidates for quantum information storage, similar to the well-known NV center in diamond.[21]

Unambiguous experimental demonstration of TEs within a single nanotube has been a challenge due to the complexity of the exciton level structure and the possible occurrence of defect state emission. For example, lower-energy emission has been observed when coating SWCNTs with EuS,[22] gold nanoparticles,[23] or palladiumporphyrins[24] that can be considered as spin filters, but its attribution to TEs has been debated as similar lower-energy emission was observed for trions or sp^3-defect sites.[12,25] More recently, the fine structure observed in low temperature magneto-PL experiments of some particular sp^3-functionalized SWCNTs was attributed to the presence of TEs,[26] and functionalization of SWCNTs with organic radicals was also found to enhance intersystem crossing (ISC) to TEs.[27] Moreover, energy transfer from singlet oxygen molecules was found to directly create TEs on nearby SWCNTs, resulting in delayed fluorescence.[28] Also other techniques such as transient absorption spectroscopy hinted at the existence of TEs,[29,30] with lower-energy absorption and long excited-state lifetimes.

However, an unambiguous proof of the existence of TEs in (6,5) SWCNTs was provided by combining optical spectroscopy with a spin-sensitive technique, namely optically detected magnetic resonance (ODMR).[31] ODMR has been extensively employed to investigate photoexcited triplet states in organic molecules. In this experiment, the sample is simultaneously subjected to optical excitation populating the triplet states, to a static magnetic field splitting up the spin levels due to the Zeeman interaction (m_s = 0, ±1, for a triplet) and to microwaves inducing transitions between these triplet states. In this way, the intensity of the samples' photoemission, which is associated with the paramagnetic excited state of interest, can be enhanced or reduced when the microwaves resonantly hit the spin transitions. The changes in light emission are then monitored as a function of magnetic field forming the ODMR spectrum. The main advantage of ODMR is its spin sensitivity to detect, on a background of the intense prompt singlet emission, a weak changing emission (of the order of 10^{-4}–10^{-5} of the singlet emission) arising either from (i) the radiative decay of an excited triplet state (thus increasing the phosphorescence),[32] (ii) ground-state recovery after (non-radiative and radiative) triplet decay (thus increasing the singlet excitation and emission),[32] or (iii) a more complex triplet to singlet conversion process, such as TTA.[31,33,34]

Stich et al. presented the ODMR spectrum of polymer-wrapped (6,5) SWCNTs drop-cast on a substrate.[31] By changing the frequency at which the microwave intensity is modulated during the experiments, to provide for phase-sensitive detection, they were able to derive a TE lifetime of 30 μs at a temperature of 5 K. By changing the intensity of the laser excitation and measuring the corresponding intensity changes of the ODMR signal, a triplet formation yield of 5% was obtained. However, the origin of the ODMR spectrum and in particular its fine structure was not investigated in detail and was preliminarily ascribed to a combination of one triplet center with rhombic symmetry and one triplet with unresolved zero-field tensor.[31,35] Following this observation, Negyedi et al. built a spectrometer to perform spectrally resolved ODMR,[36] that allows to simultaneously measure the regular PL emission and the ODMR signal of SWCNTs. Recording of the ODMR map by changing the excitation and emission wavelengths allowed for the identification of phosphorescence, and as such, the SE-TE energy difference could be determined for several SWCNT chiralities.[32] However, the study was performed at a fixed magnetic field and at relatively high temperature (77 K) such that the fine structure of the ODMR signal, consisting of signals from different TE manifolds, was not resolved.

Here, we investigate in detail the symmetry and structure of TEs in high-purity (6,5) and (7,5) single chirality samples embedded in different matrices by performing ODMR as a function of temperature and sample treatment on both randomly and in-plane preferentially oriented SWCNTs. We resolve the different components of the ODMR spectra, determine the zero-field splitting (ZFS) parameters and symmetry in the spin Hamiltonian, and relate this to different types of TEs. This work demonstrates the strength of combining the advanced methods of SWCNT separation with the powerful ODMR technique, to acquire information about TEs in SWCNTs.

RESULTS AND DISCUSSION

ODMR Sample Requirements. In an ODMR experiment, changes in SWCNT emission are probed as a function of magnetic field, while sending microwaves with a fixed frequency to the sample. Microwave-induced population changes of specific triplet spin state levels can enable/suppress direct emission from the triplet states (phosphorescence), resulting in an enhanced/decreased SWCNT emission, that additionally will result in an increased/decreased recovery of

https://doi.org/10.1021/acsnano.2c08392
ACS Nano XXXX, XXX, XXX−XXX

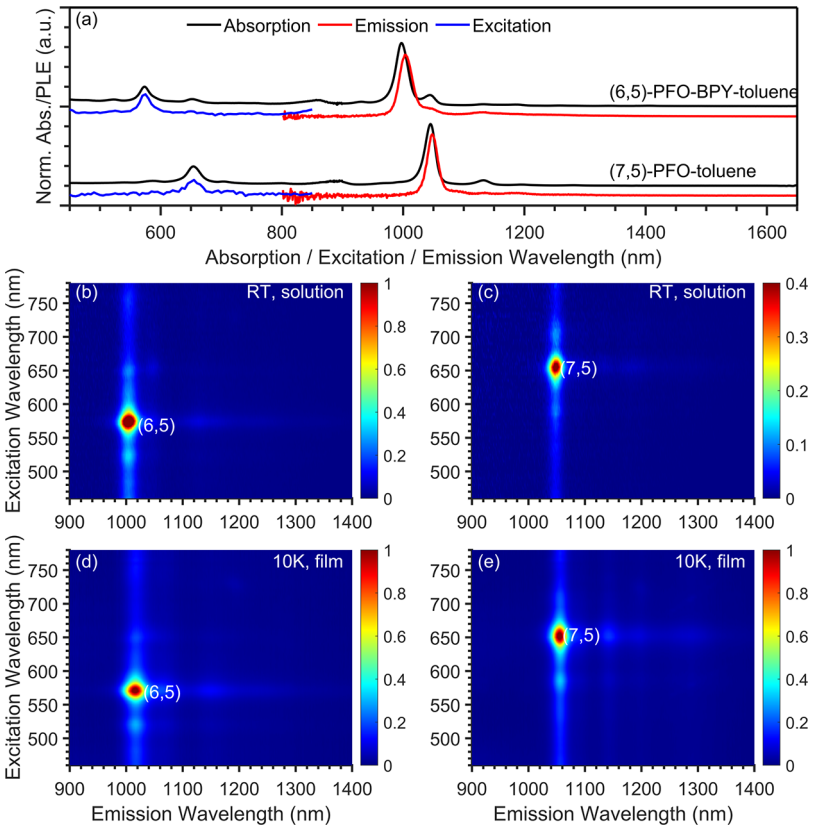

Figure 1. Absorption and PLE spectra of (6,5)-PFO-BPY-toluene and (7,5)-PFO-toluene samples. (a) Normalized absorption spectra (in black) are compared to normalized emission (in red) and excitation spectra (in blue), obtained by integrating the PLE maps over the full excitation and emission range, respectively. (b) and (c) Represent the PLE maps of the (6,5)-PFO-BPY-toluene and (7,5)-PFO-toluene solution samples at room temperature. To allow direct comparison of the PLE intensities from both solution samples, the PLE maps were divided by the maximum absorption in the original optical transition of the SWCNTs (*i.e.*, at 997 nm for (6,5) and 1045 nm for (7,5) SWCNTs). (d) and (e) Present the PLE maps of the drop-cast (6,5)-PFO-BPY-film and (7,5)-PFO-film samples acquired at low temperature (10 K). Here, the PLE intensities were first normalized to 1.

ground state population. Alternatively, it can enhance or decrease the population of the bright singlet states through TTA.[31] Palotás et al.[32] indeed found by spectrally resolved experiments that the ODMR signal consists of singlet as well as triplet emission contributions shifted with respect to each other in energy. To selectively investigate TEs from different SWCNT chiralities, it is therefore essential that the collected emission (either singlet emission or phosphorescence) stems only from the chirality under investigation. This can in principle be achieved for a sample containing a mixture of various chiralities, when spectrally resolving the ODMR signal by probing its intensity as a function of excitation and emission wavelength, similar to the approach in the more standard fluorescence−excitation (PLE) spectroscopy, thereby creating an ODMR map.[32,36] However, since in these ODMR experiments low temperatures are required, it is very difficult to keep the nanotubes perfectly isolated in a matrix. Therefore, intermolecular electronic interactions can lead to efficient exciton energy transfer[37−39] toward the lower-bandgap SWCNTs and can also influence the optical properties of the bundled nanotubes. The energy transfer of SEs can indirectly change the distribution of TEs over the different chiralities, as these TEs are mainly generated by ISC from the SEs. Meanwhile, TEs can also be directly transferred between neighboring SWCNTs as demonstrated in recent transient absorption experiments on mixtures of enriched (6,5) (donor) and (7,5) (acceptor) SWCNTs.[30] The presence of these interactions between various SWCNTs complicates the ODMR signal interpretation and therefore prevents a detailed analysis of the chirality-dependent fine structure in the ODMR spectra, such as the magnitude and symmetry of the ZFS term in the spin Hamiltonian. Moreover, it is important to investigate the influence of the nanotube environment on the localization and symmetry of the TEs, as was previously studied for the SEs, as well as on the population distribution over their spin levels.

Therefore, to unambiguously characterize the TEs in SWCNTs, we exploit the developments in postsynthesis separation of specific chiralities by aqueous two-phase extraction (ATPE)[40−42] and conjugated polymer-wrapping methods,[43−46] yielding highly pure, single-chirality solutions of isolated (6,5) and (7,5) SWCNTs, either coated by surfactants in an aqueous suspension (obtained through ATPE) or wrapped by a polymer in toluene (see the Materials and Methods section for a detailed explanation of the sample preparations). Figure 1a presents the absorption spectra of the (6,5) and (7,5) SWCNT solutions, chirality-sorted using polymer wrapping with poly-[(9,9-dioctylfluorenyl-2,7-diyl)-*alt-co*-(6,6′-[2,2′-bipyridine])] (PFO-BPY) and poly[9,9-dioctylfluorenyl-2,7-diyl] (PFO) in toluene, respectively, which can be directly compared with the emission and excitation spectra obtained from the room-temperature PLE maps of the same solutions in Figure 1b,c. These absorption and PLE spectra demonstrate that the PL detected from the samples

https://doi.org/10.1021/acsnano.2c08392
ACS Nano XXXX, XXX, XXX−XXX

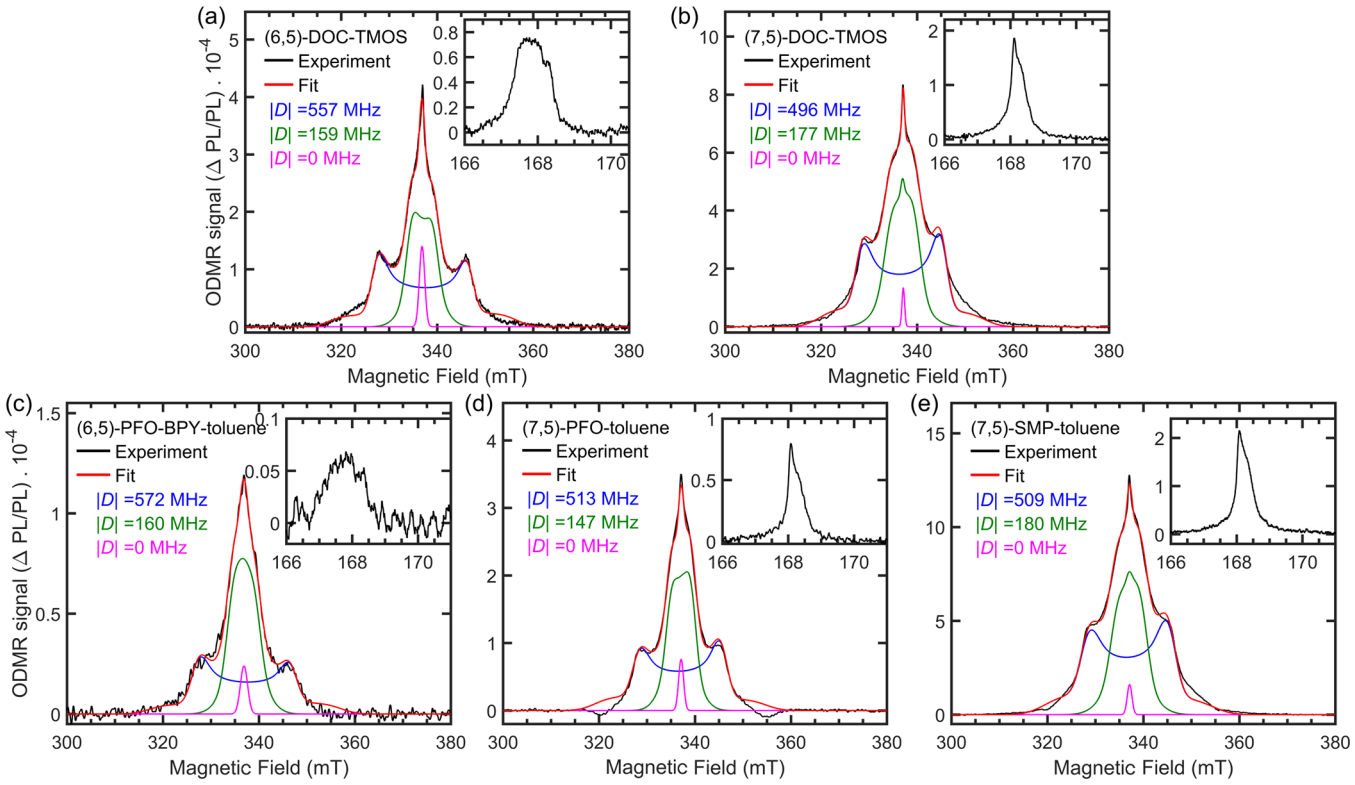

Figure 2. ODMR spectra (in black) of (a) (6,5)-DOC-TMOS, (b) (7,5)-DOC-TMOS, (c) (6,5)-PFO-BPY-toluene, (d) (7,5)-PFO-toluene, and (e) (7,5)-SMP-toluene samples recorded at a temperature of 2.5 K. Spectra were acquired with laser excitation at 561 nm for (6,5) SWCNTs and at 635 nm for (7,5) SWCNTs and an InGaAs detector, collecting both the bright SE emission and the eventual phosphorescence from the TEs. The ODMR intensity is presented by normalizing over the total emission intensity. The insets present the dipole forbidden $\Delta m_s = 2$ transitions, the so-called half-field signals. More information on the different aspects of the ODMR signal analysis can be found in the SI, Section S3. Superimposed on the ODMR spectra (in black), a simulation is presented (in red), which is composed of a superposition of 3 triplet systems, two with axial symmetry ($E = 0$) and different D-parameters (TE1 in blue and TE2 in green) and one triplet (TE3 in magenta) with unresolved ZFS ($D = E = 0$). The obtained fitted D-values are also presented in the figure in the corresponding color (see also Table 1 for the other fit parameters).

originates essentially from a single chiral species. Similar room temperature absorption spectra and PLE maps can be found in the Supporting Information (SI), Figures S1−S2, for the solutions of (7,5) SWCNTs wrapped with the 1,1′-(((1*E*,1′*E*)-(9,9,-didodecyl-9H-fluorene-2,7-diyl)bis(ethane-2,1))bis(6-methyl-4-oxo)1,4-dihydropyrimidine-5,2-diyl))bis(3-dodecylurea) polymer (SMP) and the aqueous surfactant solutions of (6,5) and (7,5) SWCNTs originating from the ATPE separation.

The ODMR experiments need to be performed at low temperature, such that relaxation rates of the different spin levels are strongly reduced. For the polymer-toluene samples, ODMR is performed by either directly freezing the toluene solution (3D randomly oriented SWCNTs) or by preparing drop-cast films of these solutions (2D randomly oriented SWCNTs in the film plane, further referred to as in-plane preferentially oriented SWCNTs). Indeed, SWCNTs will be randomly oriented when directly freezing the toluene solutions in liquid nitrogen after which the sample is transferred into the cryostat (note that freezing of the samples is thus performed in the absence of the magnetic field). Quite differently, drop-casting of the solutions will result in a preferential alignment of the long axis of the SWCNTs in the film plane, while still being randomly oriented within the plane of the film.[47] To verify the drop-casting was successful, PLE maps of the drop-cast films at room and low temperature were compared with those of the corresponding solutions. For example, in Figure S3 in the SI, the film and solution spectra for the (7,5)-PFO samples are directly compared at room temperature, showing only slight variations in peak position and line widths expected from the different external environment (polymer/toluene versus polymer alone) and thus indicating that the SWCNTs remain largely isolated in the film samples. Second, Figure 1d,e provides the low temperature PLE maps of the drop-cast films, resulting typically in small shifts of the optical transitions (of the order of 10 meV) and virtually no changes in the overall shape of the emission spectra at low temperature. Similarly as for the toluene samples, drop-cast films were also prepared from the surfactant solutions, to obtain in-plane preferentially oriented SWCNTs (see Figure S5 in the SI for their low temperature PLE maps).

In contrast, an aqueous solution of SWCNTs cannot be directly frozen as the water prevents a good glass formation. Indeed, without addition of a glassing agent, the freezing of water results in a very inhomogeneous distribution of strains exerted on the different SWCNTs, and irreversible modifications of the SWCNT samples. To prevent this, we first prepared a gel-like sample by adding 10% tetramethyl orthosilicate ($Si(OCH_3)_4$ or TMOS) to the aqueous suspension and allowing it to gel for 30 min. TMOS was selected as a glassing agent, as it does not influence the PL peak positions, line widths, or intensities with respect to the

https://doi.org/10.1021/acsnano.2c08392
ACS Nano XXXX, XXX, XXX−XXX

Table 1. Spin Hamiltonian Parameters Obtained from Fitting the Full-Field ODMR Spectra in Figure 2, Using an EPR Simulation Composed of a Sum of 3 Triplet Systems (TE1−3)[a]

	Sample/Parameters	(6,5)-DOC-TMOS	(7,5)-DOC-TMOS	(6,5)-PFO-BPY-toluene	(7,5)-PFO-toluene	(7,5)-SMP-toluene
TE1	g_1	2.0008 ± 0.0030	2.0023 ± 0.0030	2.0007 ± 0.0030	2.0013 ± 0.0030	2.0015 ± 0.0030
	$\lvert D_1\rvert$ (MHz)	556.5 ± 2.9	496.4 ± 4.0	571.7 ± 7.7	512.9 ± 4.0	508.9 ± 4.0
	σ_{D_1} (MHz)	63.8 ± 3.8	71.3 ± 4.5	68.4 ± 3.9	69.7 ± 5.1	84.9 ± 5.1
TE2	g_2	2.0019 ± 0.0030	2.0017 ± 0.0030	2.0022 ± 0.0030	2.0008 ± 0.0030	2.0013 ± 0.0030
	$\lvert D_2\rvert$ (MHz)	159.1 ± 1.9	177.4 ± 1.7	159.6 ± 3.8	146.7 ± 2.0	180.0 ± 2.0
	σ_{D_2} (MHz)	55.0 ± 2.3	76.7 ± 2.0	64.0 ± 3.0	52.6 ± 3.7	76.4 ± 3.7
TE3	g_3	2.0023 ± 0.0030	2.0007 ± 0.0030	2.0021 ± 0.0030	2.0007 ± 0.0030	2.0007 ± 0.0030
	$\sigma_{H,1-3}$ (MHz)	15.57 ± 0.60	7.51 ± 0.53	24.8 ± 4.7	14.3 ± 1.5	13.6 ± 1.5

[a]In these simulations, an isotropic *g*-tensor is assumed (as it is not resolved in the X-band ODMR spectra) as well as axial symmetry for TE1 and TE2. Line broadenings include both an intrinsic Gaussian line width (taken to be the same for all triplets for simplicity, denoted as $\sigma_{H,1-3}$), and for each of the two axial triplets, an additional Gaussian distribution of the *D*-value was used in the simulation (where σ_D, the width, *i.e.*, is defined as the standard deviation of this Gaussian distribution, meaning 68% of *D*-values lie in this range). The error bars take into account the fit errors as well as experimental accuracies, *e.g.*, the magnetic field accuracy which is dominant for the determination of the *g*-factor.

DOC solution at room temperature (as demonstrated in Figure S4 in the SI). Moreover, the TMOS gels can be reversibly frozen and warmed up without changing the ODMR signals of the SWCNTs (Figure S6 in the SI), indicating the SWCNTs remain stable in the sample upon reversible freezing, making TMOS the ideal matrix to investigate the aqueous suspensions with ODMR for a random orientation of SWCNTs. Other glassing agents like agarose gels and a poly(vinyl alcohol) matrix were also tested, but in contrast with TMOS resulted in quenched PL intensities and line broadening.

ODMR of Randomly Oriented SWCNTs. We start with ODMR measurements from frozen TMOS samples [*i.e.*, (6,5)-DOC-TMOS and (7,5)-DOC-TMOS; Figure 2a,b] and frozen toluene solutions [*i.e.*, (6,5)-PFO-BPY-toluene, (7,5)-PFO-toluene, and (7,5)-SMP-toluene; Figure 2c−e; see methods for a more detailed discussion of the sample preparation]. In these frozen samples, we can assume a random orientation of the SWCNTs, such that every possible orientation of the TEs with respect to the externally applied magnetic field is equally present. Hence, the ODMR spectrum consists of an orientation-weighted summation of all possible individual resonance contributions of many SWCNTs in different orientations relative to the static magnetic field and thus exhibits the fundamental line shape signatures of a so-called triplet powder pattern (see Section S3 and Figure S7 in the SI for more information regarding this triplet powder pattern).[48]

Figure 2 presents the triplet ODMR signals of these samples, appearing each time in two magnetic field regions, the so-called full-field region centered around the expected resonance field of spins with $g \approx 2$ (≈336 mT) and at about the half-field value [effective *g*-value $g_{eff} \approx 4$ (≈168 mT); inset of each figure panel]. The latter feature is considered as very direct evidence for triplet spin states, as it corresponds to the magnetic dipole forbidden $\Delta m_s = 2$ transition.[48] The experimental ODMR intensity is presented as the change in photoluminescence intensity (ΔPL) normalized over the emission intensity (PL) when the microwaves are not in resonance, *i.e.*, ΔPL/PL, allowing for a better comparison between different experiments (*e.g.*, with different laser excitation wavelength and power and sample-specific SWCNT PL quantum efficiencies and concentrations). As described in detail in section S3 of the SI, the broad full-field spectrum stems from the magnetic dipole−dipole interactions between the spins of electron and hole composing the TE, represented in the spin Hamiltonian by the ZFS term, which can be expressed using two independent parameters, *D* and *E*, the axial and rhombic ZFS parameters, respectively. These parameters can in general be derived from the experimental spectrum and provide information on the symmetry and localization of the electronic state (see section S3 of the SI). To this end, we employ the open-source MatLab toolbox *Easyspin* for simulating electron paramagnetic resonance (EPR) spectra,[49] which calculates the orientation-dependent transition probabilities for magnetic dipole transitions.

While at first sight, the spectra might seem to resemble those of a rhombic triplet system, as previously postulated,[31,35] such a simulation does not reproduce well the positions of all the peaks (see Figure S9 in the SI) and, moreover, cannot explain the orientation-dependent ODMR as well as the changes of the ODMR spectra as a function of temperature and sample treatment (*vide infra*). Moreover, the half-field OMDR signals all seem to contain more than one resonance position, particularly observed for the (7,5) SWCNTs, that show two relatively narrow resonances. Significantly improved simulations are obtained by assuming the spectrum is a superposition of 3 triplet systems (Figure 2 and Table 1). A first triplet (TE1), *i.e.*, the triplet with the largest ZFS (outer flanks of the experimental ODMR spectrum), can be simulated with a purely axial symmetry ($E = 0$; blue curves in Figure 2). Even when allowing the *E*-value to be varied in the fit and starting from a more rhombic symmetry, a final fit with *E* close to 0 is obtained. The orientation-dependent ODMR spectra (*vide infra*) also point out that the TE1 triplet has a purely axial symmetry, in agreement with the expected high axial symmetry of the SWCNT system. As the half-field ODMR data all contain more than one resonance line, a second triplet with significant ZFS should be present. This second triplet, TE2 (green curves in Figure 2), shows a narrower ODMR spectrum, pointing at a smaller ZFS. Because of the strong overlap with the other two triplets (TE1 and TE3), the simulations of the powder spectra cannot exclude a contribution from $E \neq 0$ for this triplet, which would result in slight variations in the center of the triplet ODMR spectra where the spectra are overlapping. Since we cannot resolve the symmetry of this triplet at this point, for simplicity *E* is assumed to be zero throughout this work. We will show later that this provides close fits of the experimental ODMR spectra also for in-plane preferentially oriented SWCNTs.

https://doi.org/10.1021/acsnano.2c08392
ACS Nano XXXX, XXX, XXX−XXX

Finally, the third contribution (TE3, magenta in Figure 2) stems from weakly interacting electron−hole pairs with minimal overlap between the spin densities of electron and hole, and thus, a small, unresolved ZFS such that the signal appears as a single narrow line, *i.e.*, $D = E = 0$ for the purpose of the analysis. This third triplet can more easily be simulated by a spin $S = 1/2$ system, reducing the number of fit parameters, analogous to the resonance of so-called distant polaron pairs observed in organic materials.[33,34,50,51] Figure 2 shows (red curves) the final simulation of the spectra as a sum of 3 triplet systems.

In addition to the above-mentioned assumptions with respect to symmetry and ZFS parameters, the origin of the ODMR line widths are also difficult to unravel with the current set of data, be it from a distribution of TEs with slightly different ZFS (inhomogeneous *D*-value distribution) or from a difference in intrinsic line width of the different TEs. For the sake of simplicity, we therefore assume the intrinsic line width of the TEs to be the same (simulated as the *H*-strain in *Easyspin*), thus mainly determined by the line width of the TE3 triplet, and simulate the additional line broadening for the TE1 and TE2 triplets as an additional inhomogeneous line broadening (*D*-strain in *Easyspin*). Since we find that *H*- and *D*-strain are highly correlated parameters, this assumption is necessary to optimize all parameters through a least-squares algorithm.

It should be noted that the relative intensities of the transitions in ODMR are not necessarily the same as the EPR transition probabilities calculated by the simulation program *Easyspin*, due to the additional processes that affect the subsequent photoemission (including ISC selectively feeding the triplet levels; radiative and nonradiative decay in the case of phosphorescence detection with corresponding ground state recovery or the TTA process, in the case of a change in SE emission,[33,51] with different probabilities for the different triplet sublevels). Indeed, it can, for example, be noticed that the outer flanks of the broad triplet ODMR spectrum for the (7,5)-PFO-toluene sample shows negative ODMR intensities, corresponding to a decrease of PL intensity as opposed to an increase in most of the spectra. These outer flanks in a powder spectrum correspond to the specific orientation of the magnetic field parallel to the D_Z-axis (see Figure S7) and thus indicates that the triplet relaxation pathways for this specific orientation of the magnetic field are different than for other orientations, thereby influencing the ODMR intensity in a different manner (see also further).

Nevertheless, taking all these aspects into account, the powder EPR triplet simulations provide a very good fit to the experimental ODMR data, allowing to fit the parameters of the spin Hamiltonian by a least-squares fitting algorithm, including the isotropic *g*-values, the *D*-parameters, and *D*-strains, *i.e.*, a Gaussian distribution of *D*-values around the central value to account for inhomogeneous broadening. Since the model does not allow for negative ODMR intensities to be included, we leave out those negative parts of the experimental data from the chi-squared minimalization when fitting the ODMR spectrum of the (7,5)-PFO-toluene sample. The spin Hamiltonian parameters (presented in Table 1), with their complex influence on each triplet spectrum, are optimized by numerical least-squares minimization using appropriate iterative procedures. At each of these iteration points, the weight factors of the three triplet spectra composing the model function are separately optimized with high gains in numerical efficiency. Indeed, as the model function is a simple linear combination of three component functions, the least-squares optimized weights can be analytically calculated using a (three-parameter) linear regression analysis.

The results in Table 1 clearly indicate that both the SWCNT chiral structure and the environment have their effect on the ZFS parameters. This also becomes clear when directly comparing the different ODMR spectra with each other by overlaying them in a single figure (see Figure S10 in the SI). When comparing the (6,5) and (7,5) TE1 triplet spectra within a similar environment, *i.e.*, those having the largest *D*-parameters (D_1, blue simulations in Figure 2), the (6,5) SWCNTs have an 11.5−12.3% larger D_1-value as compared to the (7,5) SWCNTs, which is in agreement with a tighter confinement of these excitons on the smaller-diameter (6,5) SWCNTs (see next section describing the dependence on SWCNT diameter).

Second, when comparing the ODMR spectra of a single chiral species in different environments, the TE1 triplets in the polymer-wrapped SWCNTs each time systematically show 2.7−3.3% larger D_1-values than those of the bile salt surfactants. This shows that also the environment has an influence on the localization of these TEs, though to a lesser extent than the SWCNT diameter, showing a tighter confinement in polymer-wrapped SWCNTs.

For the TE2 triplet, however, a similar systematic behavior between the different samples and environments does not occur for the observed D_2-values. As we will show further on, this triplet spectrum most likely originates from TEs trapped close to defects and therefore could be much more dependent on the exact environment and sample preparation conditions rather than on the SWCNT diameter.

Dependence of D_1 on SWCNT Diameter. The *D*-value of a molecular triplet excited state has often been related in literature to the degree of localization of the electrons. The magnetic dipole−dipole interaction between spins, also called spin−spin interaction, involves an r^{-3} dependence on the interelectronic distance *r*, from which a fast decrease of *D* can be expected as the electronic state becomes more delocalized. From their experimental *D*-value, Stich et al. estimated a radius of the TE in (6,5) SWCNTs of 0.65 nm,[31] using the equation for the radius (in nm) $r = (2.785/D)^{1/3}$ (*r* in nm, *D* in mT). Also, they argued that the spectra with smaller ZFS would therefore belong to TE states with higher delocalization. However, it is important to realize that it is not straightforward to determine the size and localization of the TEs only from the magnitude of *D*. This is evident from the basic formula for the spin−spin contribution:[52]

$$D \sim \left\langle {}^3\Psi \left| \sum_{i<j} \frac{r_{i,j}^2 - 3z_{i,j}^2}{r_{i,j}^5} \right| {}^3\Psi \right\rangle \tag{1}$$

which involves full integration over the coordinates of the electrons involved. As such, *D* depends on more than only the distance distribution between the electrons. In fact, in high-symmetry cases, with three equivalent principal directions, the ZFS parameters are found to be zero regardless of the degree of (de)localization. In the other limiting case of two well-separated localized spins, one indeed finds the simple r^{-3} relation stated earlier between distance and *D*-parameter, which is used as a ruler in distance measurements between radical groups in macromolecules.[53] But in general, for the

https://doi.org/10.1021/acsnano.2c08392
ACS Nano XXXX, XXX, XXX−XXX

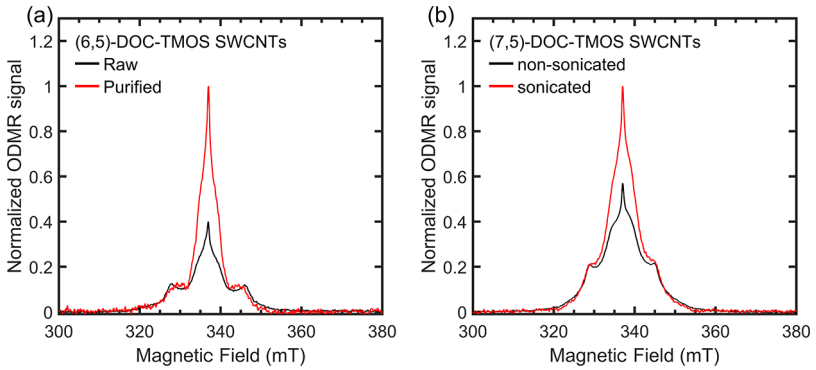

Figure 3. Normalized ODMR spectra of SWCNT samples with different sample treatments recorded at a temperature of 2.5 K with an InGaAs detector. (a) (6,5)-DOC-TMOS samples prepared from "raw" (black) or "chemically purified" (red) SWCNTs, and (b) (7,5)-DOC-TMOS samples prepared without (black) or with (red) sonication during the solubilization process. Spectra were acquired with 561 and 635 nm laser excitation for (6,5) and (7,5) SWCNTs, respectively. To better compare the spectra, each time the red spectrum was normalized and the intensity of the black spectrum was adapted to show a similar intensity of the broadest TE1 triplet, thereby showing a clear relative increase of the signal intensity of the central TEs (TE2 and TE3), hinting that the latter TEs are associated with defects.

calculation of the ZFS parameters, the specific electronic and geometrical properties of the molecular system must be carefully taken into account.

Theoretical calculations of the ZFS parameters of TEs in SWCNTs have been published by Szakacs et al.,[54] based on a semiempirical electronic model (xHUGE: extended HUbbard with GEometry optimization).[52] In this framework, the main contributions to the ZFS parameters are described in terms of parametrized two-center integrals for each conjugated C−C bond (the single-site integrals vanish). This was previously successfully applied to a series of planar aromatic molecules and to the Jahn−Teller-distorted C_{60} fullerene[55] and has the merit of showing a more detailed picture of the origin of the ZFS parameters with other possible functionalities for the size-dependence magnitude. For example, a chain of identical C−C bonds with equal distribution $1/N$ of the TE over N atoms, the sum of N terms with each a $1/N^2$ weight would lead to a $1/$ length dependence. Imagining a TE strongly localized around a zigzag SWCNT, this would correspond to an inverse proportionality with the diameter. Looking at the observed difference of (6,5) and (7,5) D_1-values and their respective diameters (0.747 and 0.817 nm; 9.3% difference), such a $1/$ diameter dependence corresponds quite well with our observations (11.5−12.3% larger values for (6,5) with respect to (7,5)). It is therefore tempting to assign the D_1-values observed for each SWCNT to a TE in which the spin density is narrowly distributed on the circumference of the SWCNT diameter and therefore inherits the axial symmetry of the SWCNT system. Note that also for self-trapped electrons on a SWCNT, such a ring-like distribution was found theoretically in the limit of small electron−phonon coupling.[56] Further investigation of the exact diameter/chirality dependence of D_1-values, including more than 2 chiral structures, will be essential to verify this conclusion.

The calculations by Szakacs et al. were an interesting exercise at a time when no experimental results were available for SWCNTs; however, a direct comparison with the current experimental data is not possible since (6,5) and (7,5) chiralities were not specifically included in that study.[54] The semiconducting nanotubes closest to our experimental cases are the (6,4) and (7,3) chiralities with values $D_{calc}^{(6,4)} = -276$ MHz (-0.0092 cm^{-1}) and $D_{calc}^{(7,3)} = -201$ MHz (-0.0067 cm^{-1}), respectively. The absolute values are of the same order of magnitude as our experimental ones (see Table 1), although significantly smaller than the $|D_1|$-values of the species with largest ZFS and larger than the $|D_2|$-values of the second TE. It is worth noting the relatively large change in *calculated* value between (6,4) and (7,3) chiralities (with nearly equal diameter: 0.683 and 0.696 nm, respectively; 1.9%), in contrast with the much smaller changes observed here experimentally for D_1 between (6,5) and (7,5), in spite of the larger diameter difference between them (9.3%). Unfortunately, these calculations do not provide a solid basis for interpretation of our results. In addition to the above remarks, the calculations were limited to unrealistically short tube length, hardly more than the diameter, and no detailed information was provided about the distribution of the TE wave function over the C atoms of the SWCNTs, leaving open questions about localization and influence of the tube edges. The semiconducting and metallic chiralities also were treated identically, which leaves one with conceptual intricacies.

In triplet EPR spectroscopy, it is well-known that the sign of the D-value can be obtained from the small, but significant difference in intensity between the left and right flanks of the triplet spectra, due to the thermal population differences between the spin levels. From our ODMR results, one would tend to conclude that the ZFS for (6,5) and (7,5) triplets have opposite signs, since for the (6,5) chirality, the transition at $B \cong 328$ mT has a higher intensity than the transition at $B \cong 346$ mT, while the opposite is true for the (7,5) SWCNTs. However, these relatively small intensity variations may be of different origin, since we are measuring ODMR and not EPR. As already discussed earlier, ODMR involves additional mechanisms that may affect the detected emission intensity. Looking back at the semiempirical calculation,[54] the negative sign of D_{calc} seems to be an intrinsic feature of the applied model, which would be challenged by the possibly opposite signs for the two species studied here. However, with no further information, it is uncertain whether the differences in intensities stem from opposite signs of the ZFS or are caused by the ODMR process itself. Therefore, we here only list the absolute value of the D-parameter.

We envisage that our data on (6,5) and (7,5) SWCNTs, and eventual future ones for other chiralities, will trigger a critical inspection and extension of the available theoretical methods for the calculation of the TE states.

https://doi.org/10.1021/acsnano.2c08392
ACS Nano XXXX, XXX, XXX−XXX

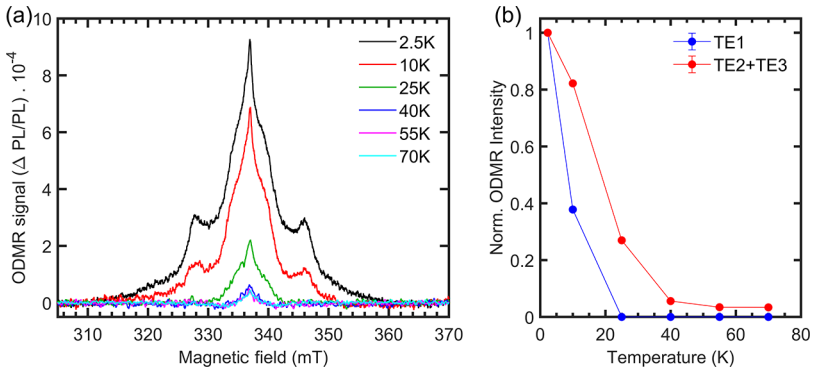

Figure 4. (a) ODMR spectra of (6,5)-DOC-TMOS samples at different temperatures, ranging from 2.5 K up to 70 K. Spectra were acquired with a 561 nm laser excitation and the InGaAs camera and a similar integration time was used for each of the spectra. (b) Normalized ODMR intensities of the TE1 contribution with respect to the summed TE2+TE3 contributions to the total ODMR spectra at different temperatures.

Influence of Sample Preparation Conditions on the ODMR Spectra. To verify that TE2 indeed stems from trapping of TEs close to defects in the SWCNT structure, we compared the ODMR spectra of two samples of (6,5)-DOC-TMOS, where the first sample was prepared from a SWCNT batch straight after synthesis (denoted as "raw" in Figure 3), while the second sample was first chemically purified by an air oxidation and acid treatment before solubilization and chiral sorting (denoted as "purified"). The chemically purified sample is expected to contain more defects, as also verified by Raman spectroscopy (see Figure S11 in the SI), which might serve as traps for the TEs at low temperature. Second, we also compare two (7,5)-DOC-TMOS samples, for which during the solubilization either sonication or no sonication was applied, thus resulting in more defects for the sonicated SWCNT samples. Figure 3 presents the comparison of the ODMR spectra of these samples normalized on the signal intensity of the TE1 triplets (D_1). This comparison clearly shows that the ODMR spectra of the chemically purified and sonicated samples (in red in Figure 3) contain a much larger relative contribution from the central TEs (TE2 and TE3), which can therefore be tentatively assigned to TEs trapped close to defects. Such a trapping of the TE2 exciton at low temperature in a potential well that is determined by the defect can also explain the quite different ZFS parameters of the TE1 and TE2 triplets. Indeed, the magnitude of the *D*-value and its symmetry are highly sensitive to the spatial overlap of the electron and hole spin density distributions. As such, one might intuitively expect a more confined triplet to show a larger ZFS; however, as shown by eq 1, a full integration over the coordinates of the electron and hole needs to be performed, and if the TE spin distribution is more isotropic, this will result in a smaller *D*-value. As pointed out above, even though we cannot resolve the exact symmetry of the TE2 triplet due to overlap with the contributions of the other two triplets, its smaller *D*-value might thus point at a less pronounced axial distortion. Future studies of particularly defect-engineered SWCNTs, such as those obtained through sp^3-functionalization,[12,13,57] could help to clarify this observation.

ODMR Spectra As a Function of Temperature. The origin of the triplet spectra can also be further verified by temperature-dependent experiments. Figure 4a presents the ODMR spectra of (6,5)-DOC-TMOS samples acquired at different temperatures. First of all, the intensity of the ODMR spectrum rapidly decreases with increasing temperature, a typical observation for triplet spin systems due to decreased spin polarization at elevated temperatures (*i.e.*, the required difference in the population of the triplet sublevels to allow for these populations to be changed by the microwaves). Figure 4b compares the intensity losses at increasing temperatures for the TE1 contribution with respect to the summed TE2+TE3 contribution, obtained by fitting the ODMR spectra with fixed ZFS parameters (those optimized at 2.5 K and presented in Table 1) and only allowing the relative amplitudes of the three different TEs to change. Since at the highest temperatures, the separate contributions of TE2 and TE3 are hard to disentangle, we present their combined intensity in Figure 4b. Interestingly, we observe distinct temperature dependences for the TEs (Figure 4b), with TE1, the broadest triplet, decreasing the fastest, while the sum of TE2 and TE3 still shows a remaining ODMR intensity even at 70 K. These distinct dependences not only support the assignment of our ODMR spectra to different TEs but the different temperature dependence also confirm that the more central triplets, TE2 and TE3, are localized at defect sites that act as a trap. This conclusion is based on the fact that the relative decrease in ODMR amplitude can be ascribed to a decrease of the steady-state population of a specific TE level. One possibility is that at increased temperature, the nonradiative recombination of the TEs increases, for example, because the TE becomes more mobile and encounters nonradiative quenching sites along the nanotubes. As the TE2 excitons are more energetically localized, the increase in nonradiative quenching will only occur at higher temperatures. If this is the case, then the ODMR signal of more localized (less mobile) TE2/TE3 excitons should decrease more slowly with increasing temperature than the delocalized (more mobile) TE1 excitons.

ODMR on Drop-Cast Films. The individual transitions constituting the ODMR spectrum are usually characterized by a narrow line width, while a powder spectrum is always much broader, as it is the sum of transitions in all possible molecular orientations. Indeed, the ODMR spectra depicted in Figures 2–4 are quite broad, which leaves ambiguity for their interpretation, in particular concerning the exact symmetry of the TEs. Conveniently, reducing the dimensionality of the system from the 3D bulk gel sample to a 2D thin film allows for a more detailed analysis of the ODMR spectrum and consequently for verification of the symmetry of the TE1 and TE2 triplets and the corresponding assignment of the ZFS parameters. For this reason, we changed the sample

https://doi.org/10.1021/acsnano.2c08392
ACS Nano XXXX, XXX, XXX−XXX

morphology by drop-casting thin SWCNT films from aqueous and from toluene solutions. In general, due to their large aspect ratio, the SWCNTs tend to lay flat on the glass substrate while evaporating the solvents, and at the same time, the projection of their long axis is randomly oriented within the film plane. This is in particular true for the drop-casting from toluene solutions, which turns out to result in a well-defined alignment of the SWCNTs in the film plane. On the contrary, drop-casting from aqueous suspension results in a less pronounced in-plane alignment and lower overall PL efficiencies (see further).

First, we investigated the drop-cast (6,5)-PFO-BPY film, of which the ODMR spectra and their respective simulations are presented in Figure 5. Spectra are acquired at intervals of 5° for

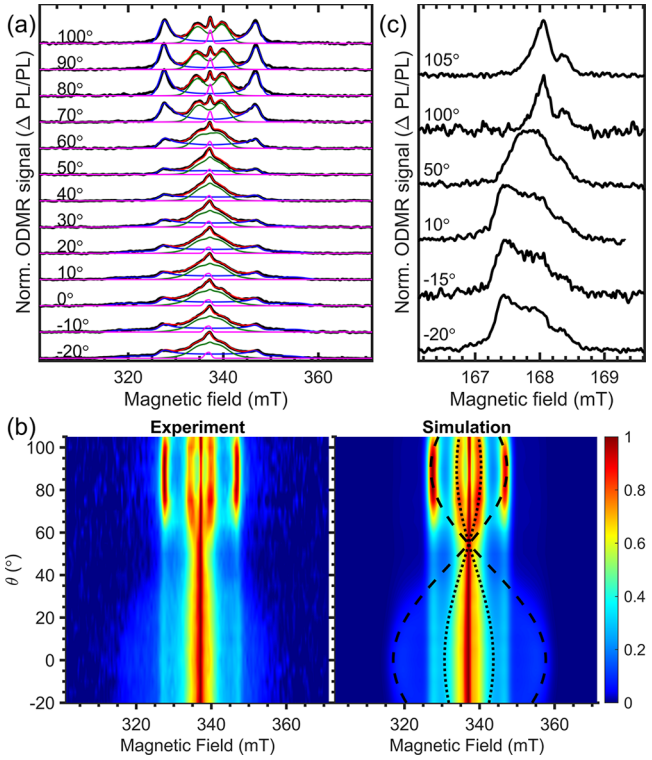

Figure 5. (a) Normalized angle-dependent ODMR spectra of the (6,5)-PFO-BPY-film with experiment (in black), total simulation (in red), and triplet contributions (in blue, green, and magenta, same color coding as in Figure 2). While ODMR spectra were acquired for intervals of 5°, we show only a selection of angles in this panel to allow for comparison between experiment and simulation. (b) Normalized ODMR intensity and simulation color map (normalized for each individual angle) of the same experimental data (here with all angles included), with superimposed the transition resonances of the two axial triplets with nonzero *D*-tensor (dashed and dotted lines for TE1 and TE2, respectively). (c) Normalized half-field angle-dependent ODMR spectra acquired at a few discrete angles, showing clear contributions from multiple triplets.

an angle θ varying from −20° to 105°, where θ represents the angle between the external magnetic field and the plane of the film, with θ = 90° corresponding to the case where the magnetic field is oriented perpendicular to the film plane. The ODMR spectral shape strongly depends on the film orientation in the external magnetic field, confirming the expected high degree of ordering of the SWCNTs in the plane of the film.[58,59] To simulate these ODMR spectra, we adopt the following assumptions and conventions, which are also represented more schematically in Figure S12 in the SI. First, the principal axis of the ZFS tensor, *i.e.*, the D_Z-axis in Figure S12, is oriented along the tube axis Z_{NT}. This is a reasonable assumption given the high axial symmetry of the SWCNT system, and in particular for the D_1 triplet due to its notable dependence on SWCNT diameter (see above). Second, we assume the SWCNTs tend to lay with their long axis, Z_{NT}, in the plane of the film, and we simulate their specific orientation with the normal on the film plane by a probability distribution which contains one single parameter, b, to express the specific distribution:

$$P(\beta) = \frac{b^2}{b^2 + (1 - b^2)\cos^2\beta} \tag{2}$$

with β the angle of the SWCNT axis with respect to the normal on the film (see Figure S12). This distribution function was previously derived and applied to fit ODMR spectra of drop-cast and spin-coated films of rigid rod-like molecules, by assuming that these molecules follow the significant reduction in one dimension of the volume elements in the solution upon drying and thereby orient themselves close to parallel to the film plane.[59] One could expect a similar behavior for much longer rod-like SWCNTs as used in this work, which was also confirmed by AFM measurements in similar drop-casted SWCNT films.[47] To allow for variability of the distribution function under different drying conditions (*e.g.*, toluene versus D_2O or starting from different SWCNT concentrations), we allow the parameter b to be adapted in the least-squares fit of the angle-dependent ODMR spectra.

In the limit b = 0 and for an orientation of the magnetic field perpendicular to the film plane (θ = 90°), the sample can effectively be treated as 2D. In this particular case, the spectrum must exhibit singularities corresponding to transitions with the field along the D_X and D_Y orientations of the ZFS tensor, since the external magnetic field **B** is in the (D_X, D_Y) plane of the nanotube reference system. Indeed, if the D_Z = Z_{NT} axis is lying perfectly in the plane, there is no contribution of the D_Z-type singularities to the ODMR spectrum (see also Figure S7). In another case, when the external magnetic field **B** lies in the plane of the film (θ = 0°), the spectrum must contain contributions from all orientations weighted with the above-mentioned probability distribution and thus should resemble more the 3D powder-like pattern, though with differently weighted contributions. As shown in Figure 5, the θ = 0° measurement closely matches the 3D powder-like spectrum, confirming the (random) orientation of CNTs in the plane of the film. Similarly as for the powder spectra, the angle-dependent ODMR spectra are simulated with a sum of 3 triplet systems, of which the parameters (*g*-tensor, *D*-tensor, *D*-strain and intrinsic line widths) and the single parameter b characterizing the orientational distribution are taken as fit parameters which are shared for all the orientation-dependent ODMR spectra, while only the angle of the external magnetic field with respect to the plane of the film is changed from one simulation to the next. Finally, to account for slight variations in the light excitation between experiments (at different angles of the film in the cavity), we furthermore allowed the relative contributions of the 3 triplet systems to vary from spectrum to spectrum. As discussed above, these amplitudes are efficiently determined by a linear regression analysis combined with the iterative optimization of the spin-Hamiltonian parameters. In principle, one expects *g*-anisotropy

https://doi.org/10.1021/acsnano.2c08392
ACS Nano XXXX, XXX, XXX−XXX

Table 2. Spin Hamiltonian Parameters and Angular Distribution Parameter b Obtained from Fitting the Full-Field Orientation-Dependent ODMR Spectra of the SWCNT Films, Using an EPR Simulation Composed of a Sum of 3 TEs[a]

Sample/Parameters	(6,5)-PFO-BPY-film	(6,5)-DOC film	(7,5)-PFO-film	(7,5)-SMP-film
g_1	1.9995 ± 0.0030	1.9999 ± 0.0030	1.9994 ± 0.0030	2.0008 ± 0.0030
$\|D_1\|$ (MHz)	568.7 ± 1.3	580.3 ± 1.8	499.5 ± 2.5	485.6 ± 3.0
σ_{D_1} (MHz)	46.7 ± 1.6	50.4 ± 3.8	63.0 ± 2.8	75.9 ± 4.2
g_2	2.0004 ± 0.0030	1.9999 ± 0.0030	2.0004 ± 0.0030	2.0010 ± 0.0030
$\|D_2\|$ (MHz)	182.2 ± 1.8	221.1 ± 4.3	190.1 ± 3.2	182.2 ± 2.8
σ_{D_2} (MHz)	79.0 ± 2.7	68.4 ± 7.4	71.2 ± 4.2	77.4 ± 4.4
$g_{3,\mathrm{perp}}$	1.9993 ± 0.0030	1.9997 ± 0.0030	2.0002 ± 0.0030	2.0034 ± 0.0030
$g_{3,\mathrm{para}}$	2.0076 ± 0.0030	2.0104 ± 0.0030	1.9968 ± 0.0060	1.9884 ± 0.0030
$\sigma_{H,1-3}$ (MHz)	9.94 ± 0.88	11.8 ± 3.5	14.3 ± 1.6	15.2 ± 1.8
Angular distribution parameter b (eq 2)	0.187 ± 0.012	0.313 ± 0.021	0.221 ± 0.020	0.644 ± 0.044

[a]In this case, the broadest 2 TEs are simulated with an isotropic g-value, an axial D-tensor, an intrinsic Gaussian line width σ_H, taken the same for all TEs, and additionally a Gaussian distribution of D-values with line width σ_D. The third TE is simulated with a slight axial g-anisotropy. The error bars take into account the fit errors as well as experimental accuracies, *e.g.*, the magnetic field accuracy which is dominant for the determination of the g-factor.

for each of the TEs, however, for TE1 and TE2 this is not observed due to the large ZFS with significant inhomogeneous broadening; therefore, the simulations are performed with isotropic g-values. For the narrow TE3 spectral feature, the orientation-dependent ODMR spectra reveal a small but significant axial anisotropy in the g-tensor, leading to an additional parameter in the global fit. The simulations of the orientation-dependent ODMR spectra thus contain only 2 additional fit parameters compared to the powder spectra, namely the orientational distribution function parameter b and the g-anisotropy, while much more experimental data are available, allowing the Hamiltonian parameters to be better defined.

Figure 5 shows the so-obtained experimental results and fits for the (6,5)-PFO-BPY-film sample, showing very good correspondence between experiment and simulations and Table 2 presents the obtained fitted parameters. As for the powder-like ODMR spectra shown in Figure 2, we do not simulate the half-field transition but show the experimental data to confirm that indeed multiple TEs with different D-values (*i.e.*, resulting in a different position of the half-field resonances) are present in the experimental data. Note that these half-field transitions, which are weaker and thus require significantly longer integration times, were only obtained for a few angles of interest (Figure 5c). Interestingly, for some of the angles, *e.g.*, $\theta = -20°$, the half-field spectra clearly show 3 transitions, while only 2 of our simulated triplets (those with nonzero D parameter) can lead to an observable half-field transition, with the transition moving to lower field position for increasing magnitude of the D-value. This indicates that the current simulation with 2 axial triplets is most likely not yet the full story. However, the already close correspondence of the full-field ODMR spectra with the simulations would not allow to introduce another triplet in our spin Hamiltonian.

Figure 6 displays the results of a similar orientation-dependent experiment for the (7,5)-PFO film with the simulated parameters also presented in Table 2. Overall, the simulations represent the experimental data very well, particularly for orientations where the magnetic field is close to perpendicular to the film plane. However, for orientations with near in-plane magnetic field alignment, negative ODMR intensities are observed at the outermost transitions, for which D_Z is near-to-parallel to the magnetic field, similarly as observed in the powder spectra.

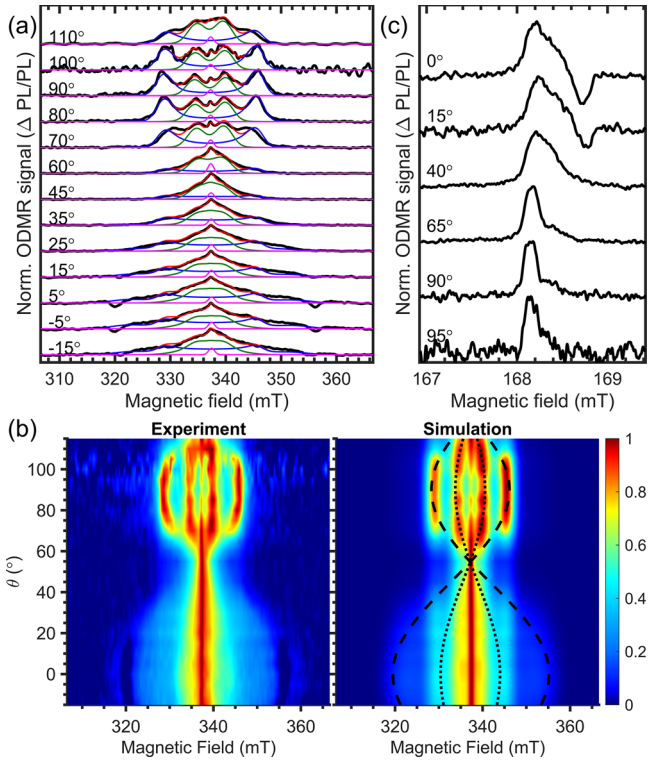

Figure 6. (a) Normalized angle-dependent ODMR spectra of the (7,5)-PFO-film with experiment in black, total simulation (in red) and triplet contributions (in blue, green and magenta, same color coding as in Figure 2). While ODMR spectra were acquired for intervals of 5°, we show only an extract of angles in this panel to allow for a decent comparison between experiment and simulation (b) Normalized ODMR intensity and simulation color map (normalized for each individual angle) of the same experimental data (here with all angles included), with superimposed transition resonances of the two axial triplets with nonzero D-tensor (dashed and dotted lines for TE1 and TE2, respectively). (c) Normalized half-field angle-dependent ODMR spectra acquired at a few discrete angles, showing clear contributions from multiple triplets, some with negative ODMR intensity.

Additionally, drop-cast films of the (7,5)-SMP sample and the surfactant-coated sample were studied, for which the results are shown in Table 2 and Figures S10–S12. For the surfactant-coated samples, the drop-casting resulted in films

https://doi.org/10.1021/acsnano.2c08392
ACS Nano XXXX, XXX, XXX−XXX

with lower optical quality, and the total emission collected from these films was rather low, thereby requiring long integration times for the ODMR experiments and thus only a few discrete angles were selected for those angular variations. Nevertheless, for the (6,5)-DOC-film, a similarly good correspondence between experiment and simulation was found as for the (6,5)-PFO-BPY-film (Figure S14), while for the (7,5)-DOC-film the signal-to-noise ratio was too low to extract decent fit parameters from the simulations (mainly due to the very low concentration of the starting solution, thereby obtaining a large ratio between the excess surfactant and SWCNTs and requiring several drops on top of each other to obtain a measurable PL signal, both resulting in a worse alignment of the SWCNTs relative to the film plane), but similarly as for the (7,5)-PFO-film, also negative intensities were found for those specific orientations where the magnetic field is oriented parallel to the SWCNT axis (*i.e.*, the D_Z -orientation, Figure S15). On the other hand, negative intensities are not observed for the (7,5)-SMP-film, but again the ODMR intensities corresponding to magnetic field aligned parallel to the D_Z-orientation do not seem to match the EPR simulations and are now a factor of 2 higher than expected (Figure S13).

When comparing the *D*-values for the film samples and the solution "powder-like" samples, slight differences are observed in the absolute numbers. Note that in theory the angular variation on the in-plane preferentially oriented SWCNT films contains more information and thus allows for a more precise determination of the *D*-values. Nevertheless, the TEs might also feel the very different local environment, with the solvent (TMOS-D_2O or toluene) no longer present in the films. Most importantly, similarly as for the powder-like spectra, a clear difference is observed between the D_1 -value for the (6,5) and (7,5) SWCNTs, hinting again at its inverse dependence on SWCNT diameter. This dependence should be further investigated using a broader range of SWCNT diameters and chiral structures. Interestingly, the slight *g*-anisotropy of the TE3 triplet is also different for the (6,5) and (7,5) SWCNTs, with (6,5) SWCNTs $g_{perp} < g_{para}$, while for (7,5), the opposite is observed, the origin of which is not yet properly understood.

It is worth considering the correspondence (and differences) between our ODMR spectra and the EPR simulations in more detail to gather information about the properties of the TEs, in particular related to photogeneration and emission and to relaxation. In general, the good agreement between the experimental spectra and EPR simulations for the (6,5) chirality, for the frozen solution as well as for the PFO-BPY-film, may be considered surprising as the simulation does not take into account the specific processes leading to ODMR. In the standard EPR simulations, thermal equilibrium is assumed for the spin sublevels, corresponding to a higher population in the lower energy triplet states. Both allowed transitions with $\Delta M_S = \pm 1$ between the spin states quantized in the static magnetic field give rise to absorption of the microwaves proportional to the population differences. However, in ODMR, the population of the triplet states depends first on the TE photogeneration rate by the ISC process from the excited singlet state and then on the decay rates *via* different pathways (radiative or not) to the singlet ground state. Both generation and decay rates are in general different for the three sublevels, which leads to steady-state unequal populations (*i.e.*, in the absence of microwaves). Consider an illustrative case (see also Figure S8) where the $M_S = 0$ triplet level is depleted compared to the $M_S = \pm 1$ levels, the quantized spin states along the static magnetic field. Microwave excitation resonant with one of the allowed transitions ($\Delta M_S = \pm 1$) will pump TEs into the (more emissive) $M_S = 0$ state, leading to an increase in phosphorescence (as $M_S = 0$ is more emissive). Simultaneously, one finds a recovery of ground state population, which is a possible mechanism for increase in fluorescence as more electrons become available again for the singlet optical cycle. (Likewise, if TTA is the dominant process to observe ODMR, *via* changes in the singlet exciton emission, the TTA efficiency can depend on the specific triplet sublevel, thus changing the population of the singlet excited states after microwave transitions change the population of the triplet sublevels.) In this example, the ODMR signal, *i.e.*, the microwave-induced change in emission, is found to be proportional to the microwave absorption, *i.e.*, the signal detected in EPR. The good fit of the spectra of the (6,5) SWCNTs, both in samples with random orientation and with in-plane preferentially oriented nanotubes, indicates that the steady-state population distribution and the preferential pathways for emission are essentially independent of field orientation relative to the nanotube axis. In the case of the (7,5) SWCNTs, a more complex situation occurs as can be seen from the negative ODMR features for the (7,5) PFO samples, observed both in frozen toluene solution and in drop-cast film, and also from the deviating intensities for the (7,5) SMP film, when the static field is parallel with the nanotube axis. This may result from a reversal of the steady-state populations, *e.g.*, when the relative depletion of the $M_S = 0$ level would be overcompensated by preferential ISC to this state, leading to a microwave-induced decrease in the emission intensity. It is interesting, however, that this happens for this singular orientation with higher symmetry (field parallel to the axial symmetry axis) where the mixing by the magnetic field of the zero-field eigenstates is vanishing, and one may expect particular selection rules for the relevant processes: ISC, (non)radiative decay, and TTA. It is intriguing that these deviating features seem to be intrinsic to the (7,5) chirality, not appearing for the (6,5) SWCNTs, which indicates differences in triplet dynamics.

In the light of the ODMR mechanisms, we also may consider two other effects observed in our measurements. First, one is tempted to determine the sign of the ZFS parameter from the difference in intensity between the two allowed transitions from $M_S = 0$ to $M_S = \pm 1$, as is well-known in standard EPR, based on the Boltzmann distribution dictating the ratio of the population differences for the two transitions, hence the ratio of intensities. In the illustrative case considered earlier, the intensities would be equal as the $M_S = \pm 1$ populations were assumed equal, a good assumption in the high-field limit as the pure quantized $M_S = \pm 1$ states are time-reversal symmetry related (and thermal population differences are negligible). In a general case, however, there will be differences in generation and decay rates for these levels that will govern the population differences in a more subtle way, not related to temperature and difficult to predict. Second, this implies that the sign of the ODMR signal in the half-field spectrum, related to the transition between $M_S = -1$ and $M_S = +1$, also depends on these subtle differences in population and on the differences in emission probabilities between these two states. In spite of this, the question arises why negative half-field signals were observed in particular for the (7,5) chirality in close to in-plane field orientations (Figure 6c). In any case,

https://doi.org/10.1021/acsnano.2c08392
ACS Nano XXXX, XXX, XXX−XXX

the exact mechanisms involved are not yet fully understood and require further investigations.

CONCLUSIONS

In conclusion, we investigated triplet excitons in (6,5) and (7,5) SWCNTs with angle-dependent ODMR spectroscopy, thereby resolving the contributions from three distinct TEs, two with different ZFS tensors and one with unresolved ZFS. By combining powder-like spectra from frozen solution with angle-dependent ODMR spectra of SWCNTs randomly oriented within the plane of a film, the symmetry of the TEs could be unambiguously determined. The one with largest ZFS (TE1) has a pronounced axial symmetry and shows an inverse proportionality dependence of the ZFS parameter on SWCNT diameter. It is therefore assigned to a TE of which the spin density is homogeneously spread on a narrow ring around the SWCNT, inheriting the SWCNTs' axial symmetry. A second triplet (TE2) has less pronounced axial symmetry, smaller ZFS parameters, and can be observed up to higher temperatures, indicating a slower increase of decay rates for those TEs, ascribed to deeper energetic stabilization. The relative abundance of these two triplets changes with sample preparation conditions (*i.e.*, chemical purification or sonication) such that we conclude that the second triplet is most likely associated with defects. Finally, a third triplet with an unresolved ZFS term in the spin Hamiltonian is also observed (TE3), very similar to the signals observed for distant polaron pairs in other organic semiconductors.

Interestingly, the ZFS values show a significant diameter dependence, while they are less sensitive to SWCNT environment (surfactant coating, polymer wrapping in solutions and films). Moreover, the ODMR intensity from (7,5) SWCNTs shows both positive and negative signals for different orientations of the SWCNT relative to the magnetic field, while for (6,5) SWCNTs, the ODMR spectra are very similar to the EPR simulations. The observation of both positive and negative ODMR signals for (7,5) SWCNTs might indicate different relaxation dynamics from the triplet spin sublevels to the ground state, thereby either increasing or decreasing the emission upon microwave absorption.

Since dark excitons, including TEs, play a significant role in the low quantum efficiency of SWCNTs, the ability to study different TEs on the same SWCNT chirality is certainly intriguing. In particular the changes in TE relaxation rates, symmetry, and ZFS tensor close to defects may be interesting in view of the ongoing search toward enhancing SWCNT emission efficiencies through sp^3-functionalization.[57] In future work, it will therefore be interesting to investigate the effect of sp^3-functionalization on triplet symmetry, ZFS tensor, and formation yield in more detail. The potential inverse dependence of the ZFS on diameter warrants further experimental and theoretical investigation across a wide range of SWCNT diameters. In particular, the very accurate determination of spin Hamiltonian parameters in this work will aid theoreticians to develop accurate models for the TEs on SWCNTs.

MATERIALS AND METHODS

Sample Preparation. *Surfactant-Based Aqueous Suspensions.* High pressure CO-conversion (HiPco)[60] SWCNTs (batch 197.2, Rice University[61]) were individually isolated by mixing with heavy water (D_2O) and 1% (10g/L) of sodium deoxycholate (DOC) surfactant. The suspension was stirred for 3 weeks using a magnetic stirring bar and intermittently sonicated 3 times for 15 min in a bath sonicator (Bransonic, 1510E-MTH, 70W, 42 kHz). After 3 weeks of stirring, a centrifugation at 16215*g* for 24 h was performed to remove any undissolved species and impurities (14000 rpm; Sigma 2-16KCH with swing-out rotor). Chirality-sorting of (6,5) and (7,5) SWCNTs was achieved by a two-step ATPE protocol as presented in refs 40 and 42, yielding aqueous samples denoted as (6,5)- or (7,5)-DOC-D_2O solutions. To compare the effect of various processing conditions, chemically purified HiPco[62] SWCNTs as well as unsonicated SWCNT samples (solubilized only by gentle stirring) were also prepared from the same HiPco batch and solubilized and sorted with the same procedures. Afterward, the samples were dialyzed to a 20 g/L DOC/D_2O solution using an ultrafiltration cell (Amicon) with 100 kDa membranes to remove the other surfactants and polymers used in the ATPE separation. To avoid bundling of the SWCNTs upon freezing of the surfactant, the solution was mixed with 10% tetramethyl orthosilicate (TMOS, Sigma-Aldrich, > 99%), which allows to fix the SWCNTs into a gel without destroying the surfactant structure around them and thus keeping the PL of the SWCNTs unchanged (see also Figure S4). These TMOS bulk samples were prepared for both the (6,5) ATPE-sorted SWCNTs as well as the (7,5) ATPE-sorted SWCNTs, which will be denoted as (6,5)- and (7,5)-DOC-TMOS. Films of (6,5) and (7,5) sorted surfactant samples were also prepared, by simply drop-casting a small aliquot of the solution on a precut glass slide and repeating this at least 4 times to obtain a film with a sufficient optical density, which will be denoted as (6,5)-DOC-film and (7,5)-DOC-film respectively.

Polymer-Wrapped Toluene Suspensions. Samples of (6,5) and (7,5) SWCNTs wrapped with different polymers and dissolved in toluene were prepared by dispersing the starting CoMoCAT SWCNT raw material (Chasm, SG65i) in toluene with either poly-[(9,9-dioctylfluorenyl-2,7-diyl)-*alt-co*-(6,6′-[2,2′-bipyridine])] (PFO-BPY) or poly[9,9-dioctylfluorenyl-2,7-diyl] (PFO) purchased from American Dye source, or 1,1′-(((1*E*,1′*E*)-(9,9,-dididecyl-9H-fluorene-2,7-diyl)bis(ethane-2,1))bis(6-methyl-4-oxo)1,4-dihydropyrimidine-5,2-diyl))bis(3-dodecylurea) (SMP) which was synthesized in house following the previously published procedure.[63] To extract (7,5) SWCNTs, we ultrasonically dispersed CoMoCat SWCNTs in PFO and toluene. PFO (22 mg) was dissolved in 10 mL of toluene while heating (70 °C). SG65i (10 mg) was suspended in the PFO solution and sonicated for 30 min using a probe sonicator operating at 40% amplitude (Cole Palmer Model CPX 750, 20 kHz). The dispersion was cooled during sonication by a surrounding bath of cool (~18 °C) flowing water. To extract (6,5) s-SWCNTs from SG65i, the SWCNTs (0.5 mg/mL) were dispersed in PFO-BPY in toluene (2 mg/mL) by tip sonication for 15 min at 40% intensity. For either sonicated dispersion, the tip-sonicated SG65i/polymer mixture in toluene was immediately transferred to a centrifuge tube following sonication, and the dispersion was centrifuged for 5 min at 13200 rpm (29760*g*) and 20 °C (Beckman-Coulter Optima L-100 XP Ultracentrifuge, SW32 Ti Rotor and Beckman-Coulter centrifuge tubes, polyallomer). A uniform SWCNT dispersion was obtained by decanting the supernatant by pipet and filtering the supernatant through a kimwipe if precipitate particles were visible in the solution.

To prepare the SMP-wrapped (7,5) SWCNTs, excess PFO in solution is first removed *via* successive centrifugation steps. The (7,5) s-SWCNT dispersion was centrifuged at 20 °C and 24100 rpm (99202*g*) for 12−20 h to remove excess polymer. The pellet, containing PFO-wrapped (7,5) SWCNTS, was separated from the supernatant, which contained excess PFO. This long centrifuge process was repeated for the redispersed pellet in toluene until the absorption of the PFO approached that of the (7,5) S_{22} excitonic transition. The pellet was then redispersed in toluene in a heated ultrasonic bath for more than an hour to yield a homogeneous (7,5)-PFO dispersion. To exchange the PFO with SMP, we then added 1 mg/mL of the SMP polymer to the homogeneous (7,5)-PFO dispersion. We then sonicated this dispersion *via* tip sonication for 15 min at 40% intensity in a bath of cool (~18 °C) flowing water, followed by centrifugation at 20 °C and 13200 rpm (29760*g*) for 5 min.

https://doi.org/10.1021/acsnano.2c08392
ACS Nano XXXX, XXX, XXX−XXX

The so-obtained solutions were either measured by directly freezing the toluene solutions, denoted as (6,5)- or (7,5)-PFO/PFO-BPY/SMP-toluene, or by drop-casting the solutions on a precut glass slide, similarly as for the surfactant films, denoted as (6,5)- or (7,5)-PFO/PFO-BPY/SMP-film.

Absorption Spectroscopy. Absorption spectra were obtained in a CARY 5000 UV−vis-NIR spectrometer using quartz microcells with a path length of 3 mm and a sample volume of 60 μL.

Photoluminescence-Excitation Spectroscopy. Two-dimensional PLE maps were collected in an in-house developed spectrometer consisting of a Xe-lamp (Edinburgh Instruments, custom adapted Xe900-XP920) for excitation and a liquid-nitrogen cooled InGaAs or extended InGaAs array detector for detecting the emission spectrum (Princeton Instruments Pylon-IR:1024 or OMA V:1024/LN-2.2). Spectra were recorded in 90° geometry in a 3 mm microcell, with 5 nm steps in excitation wavelength. Appropriate filters were used to eliminate stray light and higher order diffractions from the spectrometers, and all spectra were corrected for detector and spectrograph spectral efficiency, filter transmission, reabsorption within the cell, and (temporal and spectral) variations of the excitation light intensity. Low-temperature PLE spectra were acquired in backscattering geometry inside a Optistat CF-V cryostat (Oxford instruments) equipped with a Mercury iTC temperature controller unit and using liquid Helium as cooling agent.

Raman Spectroscopy. Raman spectra were acquired with a Dilor XY800 triple Raman spectrometer with liquid-nitrogen cooled CCD detector, under excitation at 568 and 650 nm originating from a widely tunable, frequency-doubled optical parametric oscillator (C-WAVE-GTR from Hübner Photonics).

ODMR Spectroscopy. The ODMR spectrometer is based on a continuous-wave X-band EPR spectrometer (Bruker ESP300E, 9.44 GHz) equipped with a rectangular TE102 resonator with optical access and with an Oxford liquid helium flow cryostat that can be cooled down to 2.5 K. For the randomly oriented samples, 100 μL of the TMOS-D_2O solution before gelling or 100 μL of the toluene solution was added to regular 3 mm suprasyl EPR tubes, cut in length and mounted on the end of a quartz rod, which is used for guiding the emitted light. Before mounting the samples in the cryostat and magnetic field, they were frozen in liquid nitrogen, to prevent any preferential magnetic-field induced alignment in the frozen samples. Samples were excited with laser light (using a 568 nm laser (Sapphire 568−200 CW from Coherent) or a 635 nm diode laser (MRL-III-635 nm from CNI lasers) focused on the samples through the optical window of the rectangular TE102 cavity. The emission was collected by light guiding through the quartz rod, passed through an 830 nm long-pass edge filter (BLP01-830R EdgeBasics from Semrock), and detected using a Si photodiode (S8745-01, Hamamatsu, sensitive up to 1100 nm) or a Peltier-cooled InGaAs photodiode (G12180-230A, Hamamatsu, sensitive up to 1550 nm). To collect the ODMR spectra, the microwaves were on−off modulated at a frequency of 317 Hz and subsequently introduced to the linear power amplifier (KU PA 9001250-2A, KUHNE electronics), providing a microwave output of up to 2 W. The signal from the Si photodiode was connected to a lock-in amplifier (Model 7260, EG&G Instruments) to allow for phase-sensitive detection of the ODMR signal, using the on−off modulation of the microwaves as the reference signal. ODMR spectra were each time divided by the number of scans and normalized over the total emission power coming from the sample, to allow for a direct comparison of ODMR intensities.

For angle-dependent ODMR measurements, thin films were prepared on a microscope glass substrate with an active area of 5 × 3 mm. They were either fixed inside a short EPR tube which was attached to the above-mentioned quartz rod ((6,5)-PFO-BPY-film), or mounted on the flattened side of a similar quartz rod ((7,5)-PFO-film), such that in both cases the film sample could be rotated around the axis of the rod which is perpendicular to the external magnetic field (see Figures S17−S18 in the SI for a schematic drawing of the quartz rod and the mounting of the rod in the EPR cavity).

As a reference, also the PFO and PFO-BPY polymers themselves were analyzed separately by ODMR, using different laser excitation energies but the same 830 nm long-pass edge filter. These polymers show slight fluorescence (and a narrow ODMR spectrum) passing through the filter when excited in their specific absorption peak (at 405 nm), but with the excitation wavelengths used for the SWCNT triplet investigations, no signal is observed from the polymers (Figure S16).

ASSOCIATED CONTENT

Supporting Information

The Supporting Information is available free of charge at https://pubs.acs.org/doi/10.1021/acsnano.2c08392.

Sections: (S1) absorption and PLE spectra of SWCNT samples, (S2) reproducibility of the ODMR results, (S3) ODMR theory and simulations, (S4) example scheme of the ODMR mechanism, (S5) test simulation with a rhombic triplet symmetry, (S6) comparison of (6,5) and (7,5) powder ODMR spectra in different environments, (S7) Raman spectra of the samples presented in Figure 3, (S8) ODMR on drop-cast films and their simulations, (S9) ODMR of the PFO and PFO-BPY polymer without SWCNTs, and (S10) setup and sample mounting for the ODMR experiments (PDF)

AUTHOR INFORMATION

Corresponding Author

Sofie Cambré − *Department of Physics, University of Antwerp, 2610 Antwerp, Belgium;* orcid.org/0000-0001-7471-7678; Email: sofie.cambre@uantwerpen.be

Authors

Ivan Sudakov − *Department of Physics, University of Antwerp, 2610 Antwerp, Belgium; Department of Chemistry, University of Antwerp, 2610 Antwerp, Belgium*

Etienne Goovaerts − *Department of Physics, University of Antwerp, 2610 Antwerp, Belgium;* orcid.org/0000-0002-8613-4856

Wim Wenseleers − *Department of Physics, University of Antwerp, 2610 Antwerp, Belgium;* orcid.org/0000-0002-3509-0945

Jeffrey L. Blackburn − *Materials Science Center, National Renewable Energy Laboratory, Golden, Colorado 80401, United States;* orcid.org/0000-0002-9237-5891

Juan G. Duque − *Chemistry Division, Physical Chemistry and Applied Spectroscopy Group (C-PCS), Los Alamos National Laboratory, Los Alamos, New Mexico 87544, United States*

Complete contact information is available at: https://pubs.acs.org/10.1021/acsnano.2c08392

Author Contributions

I.S. acquired and analyzed the ODMR data and performed the ODMR simulations. J.L.B. provided the polymer-sorted SWCNT samples. J.G.D. provided the HiPco SWCNTs for the aqueous samples. W.W. designed the PLE setup. S.C. performed the ATPE separations, the absorption, Raman and PLE experiments, some of the ODMR experiments, and the angle-dependent ODMR fits. E.G. and S.C. designed and supervised the ODMR experiments and data analysis. I.S., E.G., and S.C. wrote the manuscript with contributions of all authors.

Notes

The authors declare no competing financial interest.

https://doi.org/10.1021/acsnano.2c08392
ACS Nano XXXX, XXX, XXX−XXX

ACKNOWLEDGMENTS

I.S. and S.C. acknowledge funding from the European Research Council (starting grant no. 679841). Funding from the Research Foundation − Flanders (FWO Vlaanderen) is acknowledged through projects G021112N and G036618N, through a personal SB doctoral fellowship for I.S. and the EOS CHARMING project G0G6218N [EOS-ID 30467715]. This work was authored in part by the National Renewable Energy Laboratory (NREL), operated by Alliance for Sustainable Energy, LLC, for the U.S. Department of Energy (DOE) under contract no. DE-AC36-08GO28308. J.L.B. acknowledges support from the Solar Photochemistry Program, Division of Chemical Sciences, Geosciences, and Biosciences, Office of Basic Energy Sciences, U.S. Department of Energy (DOE) for polymer-wrapped SWCNT extraction and preparation. We also acknowledge the support of the Center of Integrated Nanotechnologies (CINT, Los Alamos National Laboratory, USA) for sharing the HiPco SWCNTs.

REFERENCES

(1) Avouris, P.; Freitag, M.; Perebeinos, V. Carbon-Nanotube Photonics and Optoelectronics. *Nat. Photonics* **2008**, *2* (6), 341−350.
(2) Jariwala, D.; Sangwan, V. K.; Lauhon, L. J.; Marks, T. J.; Hersam, M. C. Carbon Nanomaterials for Electronics, Optoelectronics, Photovoltaics, and Sensing. *Chem. Soc. Rev.* **2013**, *42* (7), 2824−2860.
(3) Qiu, S.; Wu, K.; Gao, B.; Li, L.; Jin, H.; Li, Q. Solution-Processing of High-Purity Semiconducting Single-Walled Carbon Nanotubes for Electronics Devices. *Adv. Mater.* **2019**, *31* (9), 1800750.
(4) Wang, F.; Dukovic, G.; Brus, L. E.; Heinz, T. F. The Optical Resonances in Carbon Nanotubes Arise from Excitons. *Science* **2005**, *308* (5723), 838−841.
(5) Maultzsch, J.; Pomraenke, R.; Reich, S.; Chang, E.; Prezzi, D.; Ruini, A.; Molinari, E.; Strano, M. S.; Thomsen, C.; Lienau, C. Exciton Binding Energies in Carbon Nanotubes from Two-Photon Photoluminescence. *Phys. Rev. B* **2005**, *72* (24), 241402.
(6) Barros, E. B.; Capaz, R. B.; Jorio, A.; Samsonidze, G. G.; Souza Filho, A. G.; Ismail-Beigi, S.; Spataru, C. D.; Louie, S. G.; Dresselhaus, G.; Dresselhaus, M. S. Selection Rules for One- and Two-Photon Absorption by Excitons in Carbon Nanotubes. *Phys. Rev. B* **2006**, *73* (24), 241406.
(7) Dresselhaus, M. S.; Dresselhaus, G.; Saito, R.; Jorio, A. Exciton Photophysics of Carbon Nanotubes. *Annu. Rev. Phys. Chem.* **2007**, *58* (1), 719−747.
(8) Crochet, J. J.; Duque, J. G.; Werner, J. H.; Lounis, B.; Cognet, L.; Doorn, S. K. Disorder Limited Exciton Transport in Colloidal Single-Wall Carbon Nanotubes. *Nano Lett.* **2012**, *12* (10), 5091−5096.
(9) Graf, A.; Zakharko, Y.; Schießl, S. P.; Backes, C.; Pfohl, M.; Flavel, B. S.; Zaumseil, J. Large Scale, Selective Dispersion of Long Single-Walled Carbon Nanotubes with High Photoluminescence Quantum Yield by Shear Force Mixing. *Carbon* **2016**, *105*, 593−599.
(10) Amori, A. R.; Hou, Z.; Krauss, T. D. Excitons in Single-Walled Carbon Nanotubes and Their Dynamics. *Annu. Rev. Phys. Chem.* **2018**, *69* (1), 81−99.
(11) Lefebvre, J.; Austing, D. G.; Bond, J.; Finnie, P. Photoluminescence Imaging of Suspended Single-Walled Carbon Nanotubes. *Nano Lett.* **2006**, *6* (8), 1603−1608.
(12) Piao, Y.; Meany, B.; Powell, L. R.; Valley, N.; Kwon, H.; Schatz, G. C.; Wang, Y. Brightening of Carbon Nanotube Photoluminescence through the Incorporation of Sp3 Defects. *Nature. Chem.* **2013**, *5* (10), 840−845.
(13) He, X.; Htoon, H.; Doorn, S. K.; Pernice, W. H. P.; Pyatkov, F.; Krupke, R.; Jeantet, A.; Chassagneux, Y.; Voisin, C. Carbon Nanotubes as Emerging Quantum-Light Sources. *Nat. Mater.* **2018**, *17* (8), 663−670.
(14) Graf, A.; Murawski, C.; Zakharko, Y.; Zaumseil, J.; Gather, M. C. Infrared Organic Light-Emitting Diodes with Carbon Nanotube Emitters. *Adv. Mater.* **2018**, *30* (12), 1706711.
(15) Danné, N.; Kim, M.; Godin, A. G.; Kwon, H.; Gao, Z.; Wu, X.; Hartmann, N. F.; Doorn, S. K.; Lounis, B.; Wang, Y.; Cognet, L. Ultrashort Carbon Nanotubes That Fluoresce Brightly in the Near-Infrared. *ACS Nano* **2018**, *12* (6), 6059−6065.
(16) Campo, J.; Piao, Y.; Lam, S.; Stafford, C. M.; Streit, J. K.; Simpson, J. R.; Hight Walker, A. R.; Fagan, J. A. Enhancing Single-Wall Carbon Nanotube Properties through Controlled Endohedral Filling. *Nanoscale Horizons* **2016**, *1* (4), 317−324.
(17) Campo, J.; Cambré, S.; Botka, B.; Obrzut, J.; Wenseleers, W.; Fagan, J. A. Optical Property Tuning of Single-Wall Carbon Nanotubes by Endohedral Encapsulation of a Wide Variety of Dielectric Molecules. *ACS Nano* **2021**, *15* (2), 2301−2317.
(18) Cambré, S.; Wenseleers, W. Separation and Diameter-Sorting of Empty (End-Capped) and Water-Filled (Open) Carbon Nanotubes by Density Gradient Ultracentrifugation. *Angew. Chemie Int. Ed.* **2011**, *50* (12), 2764−2768.
(19) Shaver, J.; Kono, J.; Portugall, O.; Krstić, V.; Rikken, G. L. J. A.; Miyauchi, Y.; Maruyama, S.; Perebeinos, V. Magnetic Brightening of Carbon Nanotube Photoluminescence through Symmetry Breaking. *Nano Lett.* **2007**, *7* (7), 1851−1855.
(20) Zampetti, A.; Minotto, A.; Cacialli, F. Near-Infrared (NIR) Organic Light-Emitting Diodes (OLEDs): Challenges and Opportunities. *Adv. Funct. Mater.* **2019**, *29* (21), 1807623.
(21) Weber, J. R.; Koehl, W. F.; Varley, J. B.; Janotti, A.; Buckley, B. B.; Van de Walle, C. G.; Awschalom, D. D. Quantum Computing with Defects. *Proc. Natl. Acad. Sci. U. S. A.* **2010**, *107* (19), 8513−8518.
(22) Mohite, A. D.; Santos, T. S.; Moodera, J. S.; Alphenaar, B. W. Observation of the Triplet Exciton in EuS-Coated Single-Walled Nanotubes. *Nat. Nanotechnol.* **2009**, *4* (7), 425−429.
(23) Harutyunyan, H.; Gokus, T.; Green, A. A.; Hersam, M. C.; Allegrini, M.; Hartschuh, A. Defect-Induced Photoluminescence from Dark Excitonic States in Individual Single-Walled Carbon Nanotubes. *Nano Lett.* **2009**, *9* (5), 2010−2014.
(24) Arellano, L. M.; Gobeze, H. B.; Gómez-Escalonilla, M. J.; Fierro, J. L. G.; D'Souza, F.; Langa, F. Triplet Photosensitizer-Nanotube Conjugates: Synthesis, Characterization and Photochemistry of Charge Stabilizing, Palladium Porphyrin/Carbon Nanotube Conjugates. *Nanoscale* **2020**, *12* (17), 9890−9898.
(25) Santos, S. M.; Yuma, B.; Berciaud, S.; Shaver, J.; Gallart, M.; Gilliot, P.; Cognet, L.; Lounis, B. All-Optical Trion Generation in Single-Walled Carbon Nanotubes. *Phys. Rev. Lett.* **2011**, *107* (18), 187401.
(26) Kim, Y.; Goupalov, S. V.; Weight, B. M.; Gifford, B. J.; He, X.; Saha, A.; Kim, M.; Ao, G.; Wang, Y.; Zheng, M.; Tretiak, S.; Doorn, S. K.; Htoon, H. Hidden Fine Structure of Quantum Defects Revealed by Single Carbon Nanotube Magneto-Photoluminescence. *ACS Nano* **2020**, *14* (3), 3451−3460.
(27) Berger, F. J.; de Sousa, J. A.; Zhao, S.; Zorn, N. F.; El Yumin, A. A.; Quintana García, A.; Settele, S.; Högele, A.; Crivillers, N.; Zaumseil, J. Interaction of Luminescent Defects in Carbon Nanotubes with Covalently Attached Stable Organic Radicals. *ACS Nano* **2021**, *15* (3), 5147−5157.
(28) Lin, C.-W.; Bachilo, S. M.; Weisman, R. B. Delayed Fluorescence from Carbon Nanotubes through Singlet Oxygen-Sensitized Triplet Excitons. *J. Am. Chem. Soc.* **2020**, *142* (50), 21189−21196.
(29) Park, J.; Deria, P.; Therien, M. J. Dynamics and Transient Absorption Spectral Signatures of the Single-Wall Carbon Nanotube Electronically Excited Triplet State. *J. Am. Chem. Soc.* **2011**, *133* (43), 17156−17159.
(30) Abudulimu, A.; Spaeth, F.; Namal, I.; Hertel, T.; Lüer, L. Chirality Specific Triplet Exciton Dynamics in Highly Enriched (6,5) and (7,5) Carbon Nanotube Networks. *J. Phys. Chem. C* **2016**, *120* (35), 19778−19784.

https://doi.org/10.1021/acsnano.2c08392
ACS Nano XXXX, XXX, XXX−XXX

(31) Stich, D.; Späth, F.; Kraus, H.; Sperlich, A.; Dyakonov, V.; Hertel, T. Triplet-Triplet Exciton Dynamics in Single-Walled Carbon Nanotubes. *Nat. Photonics* **2014**, *8* (2), 139−144.
(32) Palotás, J.; Negyedi, M.; Kollarics, S.; Bojtor, A.; Rohringer, P.; Pichler, T.; Simon, F. Incidence of Quantum Confinement on Dark Triplet Excitons in Carbon Nanotubes. *ACS Nano* **2020**, *14* (9), 11254−11261.
(33) De Ceuster, J.; Goovaerts, E.; Bouwen, A.; Dyakonov, V. Recombination of Triplet Excitons and Polaron Pairs in a Derived Paraphenylene Vinylene Pentamer. *Phys. Rev. B* **2003**, *68* (12), 125202.
(34) Dyakonov, V.; Rösler, G.; Schwoerer, M.; Frankevich, E. Evidence for Triplet Interchain Polaron Pairs and Their Transformations in Polyphenylenevinylene. *Phys. Rev. B* **1997**, *56* (7), 3852−3862.
(35) Kraus, H.Optically Detected Magnetic Resonance on Organic and Inorganic Carbon-Based Semiconductors, *Doctoral thesis*, Universität Würzburg, Würzburg, Germany, 2014.
(36) Negyedi, M.; Palotás, J.; Gyüre, B.; Dzsaber, S.; Kollarics, S.; Rohringer, P.; Pichler, T.; Simon, F. An Optically Detected Magnetic Resonance Spectrometer with Tunable Laser Excitation and Wavelength Resolved Infrared Detection. *Rev. Sci. Instrum.* **2017**, *88* (1), 013902.
(37) Qian, H.; Georgi, C.; Anderson, N.; Green, A. A.; Hersam, M. C.; Novotny, L.; Hartschuh, A. Exciton Energy Transfer in Pairs of Single-Walled Carbon Nanotubes. *Nano Lett.* **2008**, *8* (5), 1363−1367.
(38) Li, Y.; Yang, J.; Yang, N.; Zhang, D.; Wang, X.; Li, Y. Photoluminescence from Exciton Energy Transfer of Single-Walled Carbon Nanotube Bundles Dispersed in Ionic Liquids. *J. Phys. Chem. C* **2012**, *116* (41), 22028−22035.
(39) Mehlenbacher, R. D.; McDonough, T. J.; Grechko, M.; Wu, M. Y.; Arnold, M. S.; Zanni, M. T. Energy Transfer Pathways in Semiconducting Carbon Nanotubes Revealed Using Two-Dimensional White-Light Spectroscopy. *Nature Commun.* **2015**, *6*, 1−7.
(40) Subbaiyan, N. K.; Cambré, S.; Parra-Vasquez, A. N. G.; Hároz, E. H.; Doorn, S. K.; Duque, J. G. Role of Surfactants and Salt in Aqueous Two-Phase Separation of Carbon Nanotubes toward Simple Chirality Isolation. *ACS Nano* **2014**, *8* (2), 1619−1628.
(41) Fagan, J. A. Aqueous Two-Polymer Phase Extraction of Single-Wall Carbon Nanotubes Using Surfactants. *Nanoscale Adv.* **2019**, *1* (9), 3307−3324.
(42) Subbaiyan, N. K.; Parra-Vasquez, A. N. G.; Cambré, S.; Cordoba, M. A. S.; Yalcin, S. E.; Hamilton, C. E.; Mack, N. H.; Blackburn, J. L.; Doorn, S. K.; Duque, J. G. Bench-Top Aqueous Two-Phase Extraction of Isolated Individual Single-Walled Carbon Nanotubes. *Nano Res.* **2015**, *8* (5), 1755−1769.
(43) Nish, A.; Hwang, J.-Y.; Doig, J.; Nicholas, R. J. Highly Selective Dispersion of Single-Walled Carbon Nanotubes Using Aromatic Polymers. *Nat. Nanotechnol.* **2007**, *2* (10), 640−646.
(44) Guillot, S. L.; Mistry, K. S.; Avery, A. D.; Richard, J.; Dowgiallo, A.-M.; Ndione, P. F.; van de Lagemaat, J.; Reese, M. O.; Blackburn, J. L. Precision Printing and Optical Modeling of Ultrathin SWCNT/C60 Heterojunction Solar Cells. *Nanoscale* **2015**, *7* (15), 6556−6566.
(45) Ferguson, A. J.; Reid, O. G.; Nanayakkara, S. U.; Ihly, R.; Blackburn, J. L. Efficiency of Charge-Transfer Doping in Organic Semiconductors Probed with Quantitative Microwave and Direct-Current Conductance. *J. Phys. Chem. Lett.* **2018**, *9* (23), 6864−6870.
(46) Arias, D. H.; Sulas-Kern, D. B.; Hart, S. M.; Kang, H. S.; Hao, J.; Ihly, R.; Johnson, J. C.; Blackburn, J. L.; Ferguson, A. J. Effect of Nanotube Coupling on Exciton Transport in Polymer-Free Monochiral Semiconducting Carbon Nanotube Networks. *Nanoscale* **2019**, *11* (44), 21196−21206.
(47) Mirka, B.; Rice, N. A.; Williams, P.; Tousignant, M. N.; Boileau, N. T.; Bodnaryk, W. J.; Fong, D.; Adronov, A.; Lessard, B. H. Excess Polymer in Single-Walled Carbon Nanotube Thin-Film Transistors: Its Removal Prior to Fabrication Is Unnecessary. *ACS Nano* **2021**, *15*, 8252.
(48) Telser, J.EPR Interactions - Zero-Field Splittings. In *eMagRes.*; Major Reference Works; John Wiley & Sons, Ltd: Chichester, UK, 2017; pp 207−234.
(49) Stoll, S.; Schweiger, A. EasySpin, a Comprehensive Software Package for Spectral Simulation and Analysis in EPR. *J. Magn. Reson.* **2006**, *178* (1), 42−55.
(50) Lane, P.; Wei, X.; Vardeny, Z. Spin and Spectral Signatures of Polaron Pairs in π-Conjugated Polymers. *Phys. Rev. B - Condens. Matter Mater. Phys.* **1997**, *56* (8), 4626−4637.
(51) Väth, S.; Tvingstedt, K.; Baumann, A.; Heiber, M. C.; Sperlich, A.; Love, J. A.; Nguyen, T. Q.; Dyakonov, V. Triplet Excitons in Highly Efficient Solar Cells Based on the Soluble Small Molecule P-DTS(FBTTh2)2. *Adv. Energy Mater.* **2017**, *7* (7), 1602016.
(52) Bennati, M.; Németh, K.; Surján, P. R.; Mehring, M. Zero-field-splitting and Π-electron Spin Densities in the Lowest Excited Triplet State of Oligothiophenes. *J. Chem. Phys.* **1996**, *105* (11), 4441−4447.
(53) Jeschke, G. DEER Distance Measurements on Proteins. *Annu. Rev. Phys. Chem.* **2012**, *63* (1), 419−446.
(54) Szakács, P.; Szabados, Á.; Surján, P. R. Zero-Field-Splitting in Triplet-State Nanotubes. *Chem. Phys. Lett.* **2010**, *498* (4), 292−295.
(55) Surján, P. R.; Németh, K.; Bennati, M.; Grupp, A.; Mehring, M. Zero-Field-Splitting in the Lowest Triplet State of C60. *Chem. Phys. Lett.* **1996**, *251* (1), 115−118.
(56) Bratek, L.; Brizhik, L.; Eremko, A.; Piette, B.; Watson, M.; Zakrzewski, W. Self-Trapped Electron States in Nanotubes. *Phys. D Nonlinear Phenom.* **2007**, *228* (2), 130−139.
(57) Zaumseil, J. Luminescent Defects in Single-Walled Carbon Nanotubes for Applications. *Adv. Opt. Mater.* **2022**, *10* (2), 2101576.
(58) Dyakonov, V.; Kraus, H.; Sperlich, A.; Magerle, R.; Zerson, M.; Dehnert, M.Interplay Between Microscopic Structure and Intermolecular Charge-Transfer Processes in Polymer−Fullerene Bulk Heterojunctions. In *Elementary Processes in Organic Photovoltaics*; Springer, Cham, 2017; Vol. *272*, pp 139−155.
(59) Cambré, S.; De Ceuster, J.; Goovaerts, E.; Bouwen, A.; Detert, H. Quantitative Evaluation of the Preferential Orientation of Para-Phenylene Vinylene Pentamers in Polystyrene Films by Optically Detected Magnetic Resonance. *Appl. Magn. Reson.* **2007**, *31* (3-4), 343.
(60) Nikolaev, P.; Bronikowski, M. J.; Bradley, R. K.; Rohmund, F.; Colbert, D. T.; Smith, K. A.; Smalley, R. E. Gas-Phase Catalytic Growth of Single-Walled Carbon Nanotubes from Carbon Monoxide. *Chem. Phys. Lett.* **1999**, *313* (1−2), 91−97.
(61) Duque, J. G.; Parra-Vasquez, A. N. G.; Behabtu, N.; Green, M. J.; Higginbotham, A. L.; Price, B. K.; Leonard, A. D.; Schmidt, H. K.; Lounis, B.; Tour, J. M.; Doorn, S. K.; Cognet, L.; Pasquali, M. Diameter-Dependent Solubility of Single-Walled Carbon Nanotubes. *ACS Nano* **2010**, *4* (6), 3063−3072.
(62) Rai, P. K.; Pinnick, R. A.; Parra-Vasquez, A. N. G.; Davis, V. A.; Schmidt, H. K.; Hauge, R. H.; Smalley, R. E.; Pasquali, M. Isotropic−Nematic Phase Transition of Single-Walled Carbon Nanotubes in Strong Acids. *J. Am. Chem. Soc.* **2006**, *128* (2), 591−595.
(63) Pochorovski, I.; Wang, H.; Feldblyum, J. I.; Zhang, X.; Antaris, A. L.; Bao, Z. H-Bonded Supramolecular Polymer for the Selective Dispersion and Subsequent Release of Large-Diameter Semiconducting Single-Walled Carbon Nanotubes. *J. Am. Chem. Soc.* **2015**, *137* (13), 4328−4331.

https://doi.org/10.1021/acsnano.2c08392
ACS Nano XXXX, XXX, XXX−XXX